



Contents lists available at ScienceDirect

Journal of Fluids and Structures

journal homepage: www.elsevier.com/locate/jfs



Viscous fluid–flexible structure interaction analysis on ship springing and whipping responses in regular waves

Jialong Jiao ^{a,b}, Songxing Huang ^a, C. Guedes Soares ^{b,*}

^a School of Civil Engineering and Transportation, South China University of Technology, Guangzhou, 510641, China

^b Centre for Marine Technology and Ocean Engineering (CENTEC), Instituto Superior Técnico, Universidade de Lisboa, 1049-001, Lisbon, Portugal



ARTICLE INFO

Article history:

Received 15 March 2021

Received in revised form 22 June 2021

Accepted 6 August 2021

Available online 24 August 2021

Keywords:

Ship hydroelasticity

Wave loads

Springing response

Slamming and whipping

Fluid structure interactions

CFD–FEA two-way coupling

ABSTRACT

A two-way fluid structure interaction (FSI) of CFD–FEA numerical method is adopted to predict ship motions, wave loads and hydroelastic responses in regular waves. In the FSI algorithm, the external fluid loads obtained from the CFD model and the motions and structural deformations obtained from the FEA model are exchanged between each other in an iteratively staggered implicit coupling regime in time domain. The motions, vertical accelerations and wave loads including springing and whipping responses of a flexible S175 container ship under different regular wave conditions predicted by the FSI co-simulation method are systematically analyzed. High order hull girder vertical vibrations of up to 12th order harmonic springing and up to 4-node whipping responses have been successfully reproduced, which indicates that the CFD–FEA co-simulation method is reliable and capable in simulating ship nonlinear hydroelastic responses in waves. Moreover, some complex flow phenomena such as slamming, green water on deck, wave breaking and splashing have also been well reproduced from the CFD simulation. It is believed that the present FSI method will exhibit significant advantage over the traditional ways used for ship seakeeping and hydroelasticity analyses.

© 2021 Elsevier Ltd. All rights reserved.

1. Introduction

Modern ships are becoming larger and faster in order to meet the increasing demand of transportation or operational capabilities. The increase of main dimensions makes ships more flexible, and the requirement of high navigational speed leads the wave encounter frequency closer to the wetted natural frequency of ships. The two-node wetted natural frequency of vertical bending mode for large ships could be as low as encounter frequency even in an ordinary service sea state (Zhu et al., 2011). Therefore, hydroelastic effects and the relevant loads should be considered in the determination of design wave loads and structural strength evaluation of large ships (Hirdaris et al., 2014). It is known that springing and whipping are the two fundamental hydroelastic vibrations in ships (Lee et al., 2011a). The magnitude of springing loads is usually low and thus springing is normally not an ultimate strength issue. However, springing could significantly contribute to the fatigue damage of hull structure since the number of cycles can be very large during ship whole service life (Han et al., 2017). On the other hand, enormous whipping loads are usually driven by fierce bow or stern flare and bottom slamming (Wang and Guedes Soares, 2016a,b) and the oscillations usually decay rapidly due to the fluid and

* Corresponding author.

E-mail address: c.guedes.soares@centec.tecnico.ulisboa.pt (C. Guedes Soares).

structural damping effects. Thus, whipping is primarily an ultimate strength issue, which may cause transient failure of global ship hull or local structures (Lee et al., 2012; Corak et al., 2018).

Following the pioneering work of Bishop and Price (1979), there has been substantial work on both 2D and 3D hydroelasticity theory within the framework of potential flow theory. The 2D ship hydroelasticity theory was first developed on the basis of strip theory and linear beam vibration model (Bishop et al., 1986). Wu (1984) extended the 2D hydroelasticity theory to 3D by establishing the boundary condition of flexible body with respect to the fluid domain. To date, both 3D frequency-domain and time-domain linear or nonlinear hydroelasticity theories are widely adopted in the field of naval architecture and ocean engineering (Hirdaris and Temarel, 2009). To represent ship large-amplitude motion in steep waves, different levels of nonlinearity ranging from the linear, Froude–Krylov weakly nonlinear, body nonlinear to body exact (weak-scatterer method) have been developed for 3D time-domain hydroelasticity theory (Singh and Sen, 2007). Moreover, transient free surface Green's function (Li et al., 2015; Datta and Guedes Soares, 2020), Rankine source (Kim et al., 2009; Tang et al., 2020) and even their hybrid matching (Liu and Papanikolaou, 2011; Li et al., 2020) methods have been used to account for forward speed effects in the accurate solution of boundary integral equations. In addition, Wagner theory and momentum theory are also used to calculate the sectional slamming loads which can be coupled with the hydroelastic motion equation (Drummen et al., 2009; Malenica and Derbanne, 2014; Rajendran and Guedes Soares, 2016; Wang and Guedes Soares, 2017; Jiao et al., 2020). However, the flow field during slamming and green water event is highly nonlinear and cannot be accurately represented using potential flow methods (Wang and Guedes Soares, 2016a,b).

The hydroelasticity theory established under the framework of potential flow theory is however incapable of simulating some strongly nonlinear fluid structure interactions (FSI) problems. The advent of high-performance computation technique over the recent years has resulted in rapid development and implementation of fully nonlinear time-domain CFD methods to simulate 3D hydrodynamic problems of ships and offshore structures (Tezdogan et al., 2016; Wang and Wan, 2020; Huang et al., 2021a). For example, Xie et al. (2020) and Wang and Guedes Soares (2013) calculated the asymmetrical slamming loads on hull sections by CFD. Jiao and Huang (2020), Huang et al. (2021a) and Jiao et al. (2021) calculated ship seakeeping performance and slamming loads in both uni-directional regular waves and bi-directional cross-waves by RANS method. Guo et al. (2014) predicted added resistance and ship motion of KVLCC2 ship in head waves with RANS solver. Islam et al. (2019) calculated the wave radiation of a box-type floating structure by OpenFOAM. Hashimoto et al. (2020) predicted the wave-induced global forces and moments on ships in irregular stern quartering seas by integrating the local elemental forces along the hull surface. Although global motions and external loadings can be routinely obtained by CFD simulation, the hull sectional loads, e.g. vertical bending moment and shear force, used for wave loads analysis cannot be directly obtained from the CFD simulation. Moreover, the majority of current CFD applications are limited to simulating fluid flow around a rigid body.

Over the past several years, simulations of fluid–flexible structure interactions (FFSI) using CFD technique has gained significant interests. To obtain the fluid loadings and flexible deformations of structures, finite element analysis (FEA) for structural part is used to couple with the CFD solver of fluid solution. For example, Paik and Carrica (2014) employed a CFD–FEA fully coupled approach to study the rolling tank motions including the free-surface effects and good agreement was found with the experimental data. Lee et al. (2017) investigated the hydroelastic behavior of a composite propeller using CFD–FEA method for FSI analysis. Bakica et al. (2020) presents a novel methodology of the load transfer based on the projection method for the specific application to CFD hydrodynamic and FEA structural coupling. Pernod et al. (2019) performed experimental analysis of the composite hydrofoil in flow and also compared the experimental data with the CFD–FEA numerical method. Sun et al. (2020) investigated the motion, structural response and cavitation bubble evolution of a cylinder entering into water at high speed using a CFD–FEA coupled method. Huang and Chen (2020) investigated vortex-induced motion of a deep draft semi-submersible by coupled CFD–FEM analysis.

Moreover, the CFD–FEA coupled method has also been used to study the wave-induced loads and hydroelastic responses of flexible ships. For example, Lakshmynarayanan and Hirdaris (2020) and Lakshmynarayanan and Temarel (2020) investigated the symmetric motions and loads on a S175 container ship undergoing severe waves and slamming impacts by both one-way and two-way CFD–FEA coupling methods. Mohtar et al. (2017) presented a computational method by solving RANS equations coupled with nonlinear vibration equations of elastic ship hull to assess slamming-induced hull whipping loads in both regular and irregular waves. McVicar et al. (2018) developed one-way and two-way interaction methods considering vibration of hull girder to calculate the slamming and whipping loads on high-speed wave-piercing catamarans. Ma and Mahfuz (2012) modeled a ship hull with sandwich composite structure by using ANSYS and solved the fluid flow by CFX and coupled them using the ANSYS Workbench platform. All these works suggest that the high frequency hydroelastic vibrations cannot be directly simulated in the one-way coupling method since the structural deformation of hull is not considered in the CFD simulation. Thus, the two-way coupling is more accurate to reproduce the hydroelastic effects of flexible ship in waves.

Although the CFD–FEA coupling method has been used to predict ship hydroelastic responses in some literature, the related numerical technique is immature and still needs to be further applied and refined owing to its high superiority and potential application values compared with the classical potential flow theory. The interest of the present work lies in the investigation of springing and whipping loads acting on a flexible ship by the co-simulation method. For this purpose, a two-way coupling of CFD–FEA numerical method is applied to predict the motions, wave loads and hydroelastic vibrations of a S175 container ship in waves. Some high-order harmonic springing and whipping responses are satisfactorily reproduced, which suggests that the present FSI co-simulation method is reliable and insightful in hydroelastic analysis of ships and floating structures.

Table 1
Main dimensions of the S175 container ship.

Item	Full-scale	Model
Scale	1:1	1:40
Length between perpendiculars (L)	175 m	4.375 m
Breadth (B)	25.4 m	0.635 m
Depth (D)	19.5 m	0.488 m
Draft (T)	9.5 m	0.238 m
Displacement (Δ)	23,711 t	370 kg
Block coefficient (C_B)	0.562	0.562
Midship section coefficient (C_M)	0.990	0.990
Prismatic coefficient (C_p)	0.568	0.568
Longitudinal center of gravity from AP (x_{cog})	84.980 m	2.125 m
Vertical center of gravity from keel (z_{cog})	8.5 m	0.213 m
Longitudinal radius of gyration (k_{yy})	42.073 m	1.052 m

Compared with the state of the art on CFD–FEA coupling simulation of ship hydroelasticity, e.g. [Lakshmynarayana and Hirdaris \(2020\)](#), this study reproduces almost all the physical characteristics of interests within the scope of ship seakeeping and hydroelasticity including large-amplitude motions, accelerations, wave loads, slamming loads, green water, springing and whipping responses. The present method can be extended to address bending-torsional coupling loads of ship in oblique regular waves and in long-crested and even short-crested irregular waves ([Huang et al., 2021a](#)). Moreover, compared with the work in [Lakshmynarayana and Hirdaris \(2020\)](#), more detailed time-domain and frequency-domain data of ship motions and loads obtained by the CFD–FEA coupling method are presented and analyzed in the present study. The global motions, wave loads and springing and whipping responses of the ship in different regular head wave conditions are comprehensively analyzed and also compared with some existing tank model experimental ([Watanabe et al., 1989; Chen et al., 2001; Fonseca and Guedes Soares, 2004a,b](#)) and numerical ([ISSC, 2000; Lakshmynarayana and Temarel, 2020](#)) results of the S175 ship.

2. Numerical method and model setup

In this study, a standard S175 container ship is used for modeling, simulation and data analyses. A two-way interaction simulation method is adopted by combining the CFD solver STAR-CCM+ and the FEA solver ABAQUS with the help of the SIMULIA co-simulation engine in an iteratively staggered coupling regime. The FSI co-simulation method and the details in numerical model setup using the S175 ship are reported in this section.

2.1. Ship model description

The S175 container ship is well known because it was used by the International Towing Tank Conference (ITTC) and International Ship and Offshore Structures Congress (ISSC) communities to carry out comparative studies of linear wave-induced motions and sectional loads. The ship motions and wave loads simulations were applied to a S175 container ship model with a 1:40 scale ratio. A naked hull body with a flat main deck is adopted for the seakeeping investigation. The rudder, propeller and bilge keels are not appended. Main dimensions of the ship prototype and the model are presented in [Table 1](#). The transverse body plan of the ship hull is shown in [Fig. 1](#). Middle longitudinal plane of the ship hull and the locations of each station are shown in [Fig. 2](#). In the figure, the green line denotes a backbone beam and the blue circles denote nodes of the beam element, which will be described in Section 2.3.1 in detail.

The ship model has 21 stations (marked by vertical gray lines in [Fig. 2](#)) with station 0 and 20 coinciding with the aft perpendicular (AP) and forward perpendicular (FP), respectively. For the investigation of wave loads and whipping responses, sectional loads at center of each segment are monitored, i.e. at sections from #1 to #20 (marked by vertical red line in [Fig. 2](#)). Longitudinal distribution of mass along the model hull is shown in [Fig. 3](#). The vertical bending stiffness ($EI = 9.88 \times 10^4 \text{ N m}^2$) of the model is assumed to be constant longitudinally and the value was determined to meet the two-node natural frequency of vertical bending vibration of hull.

2.2. Hydrodynamic solver

Finite volume method (FVM) is used to model the fluid domain and the free surface is captured by volume of fluid (VOF) technique. The fluid flow is represented by solving the unsteady Reynolds averaged Navier–Stokes (URANS) equations. A second-order upwind scheme is used throughout all simulations to discretize the convection term. The segregated flow model that solves the flow equation in an uncoupled manner with the help of staggered grids is applied. The overall solution procedure is obtained according to a Semi-Implicit Pressure Linked Equations (SIMPLE) type algorithm to achieve an implicit coupling between pressure and velocity, which uses a predictor–corrector approach to link the continuity and momentum equations. The turbulence model of Realizable $k-\varepsilon$ which is very suitable for solving external flow with large streamline curvature such as the flow around the hull is adopted in this study. Generally, the influence of different

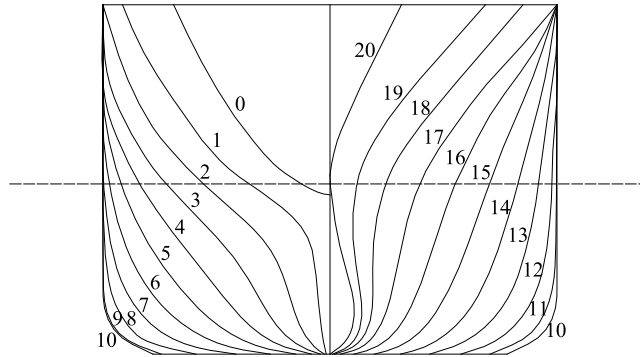


Fig. 1. Transversal body plan of the S175 hull.

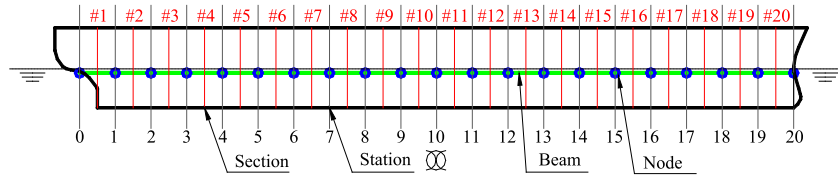


Fig. 2. Arrangement of ship model viewed from middle longitudinal plane.

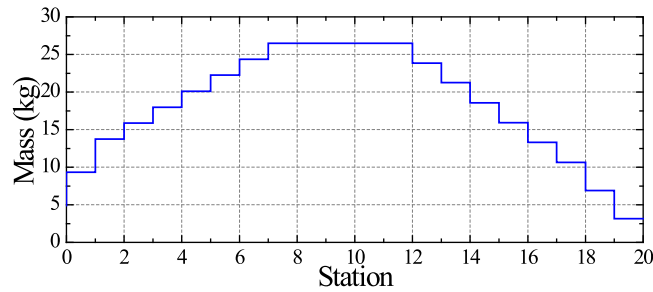


Fig. 3. Longitudinal distribution of mass in model scale.

turbulence model on ship seakeeping results is very small. A comprehensive discussion on the application of different eddy-viscosity turbulence models to problems in ship hydrodynamics can be found in Terziev et al. (2020). It is noted that the laminar model can be also used to solve the ship hydrodynamic problems and reasonable results can be obtained compared with the turbulence model (Gao et al., 2018; Liu et al., 2020). The High Resolution Interface Capturing (HRIC) scheme is employed to ensure a sharp interface and requires that Courant numbers at the free surface be strictly controlled to prevent smearing of the water and air phases at their interface.

2.2.1. Fluid domain and boundary conditions

A numerical wave tank is established with the help of STAR-CCM+ software (CD-Adapco, 2019). The origin of coordinate system is located at the intersection of the following three orthogonal planes: the free-surface of calm water, the middle longitudinal symmetric plane and the transverse cross section at AP of the hull. The longitudinal direction of the ship is aligned with the x -axis, the side wall extended in the y -axis, and the air extended in the z -axis which points to the sky. A general view of the computational fluid domain with the hull model and the notation of selected boundary conditions are depicted in Fig. 4. Overset grid technique is used to simulate ship large amplitude motions in waves. For this purpose, two different regions including the background and overset regions are created. The overset region is attached to the hull body and moves with it freely in the background region.

Due to the symmetry of ship responses in head waves, only half of the fluid field is created as the computational domain with a symmetry plane being adopted to reduce the calculation cost. The extent of the whole computational domain is $-8.75 < x < 11$ m, $0 < y < 6.6$ m, $-10 < z < 5$ m, which are determined by referring to the recommendations of ITTC (2011). The extent of the overset region is $-0.4 < x < 4.7$ m, $0 < y < 0.6$ m, $-0.4 < z < 0.45$ m. To be different from the commonly used damping wave method for wave generation and elimination (Guo et al., 2014; Deng et al., 2019), the Euler Overlay Method (EOM) is applied in the present CFD simulation (Takami et al., 2018; Choi and Yoon, 2009). Therefore, the

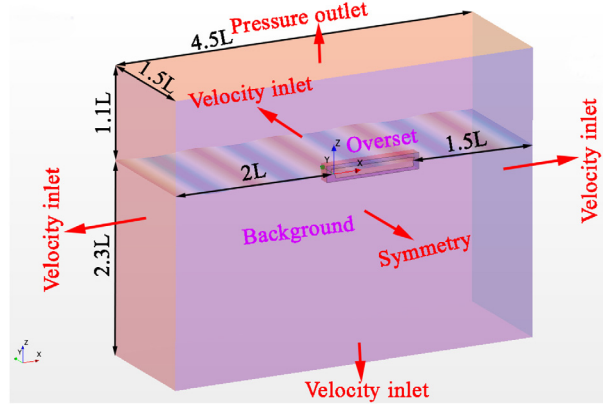


Fig. 4. Summary of the boundaries of the numerical wave tank.

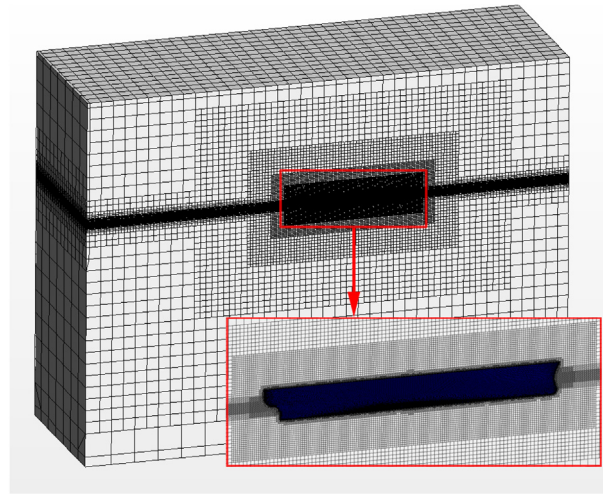


Fig. 5. 3D view of the computational grid.

boundary conditions of the fluid domain are set as follows. Velocity inlet is applied at the vertical boundaries (including wave inlet, wave outlet and side wall) and bottom of the fluid domain so as to define the fluid velocity on these boundary conditions as required. Pressure outlet is applied at the top boundary to present the static pressure in the sky. No-slip wall is applied at the ship body surface where the fluid tangential velocity is zero.

2.2.2. Mesh generation

Mesh generation is performed by using the automatic meshing facility in STAR-CCM+. A trimmed cell mesher is adopted to produce a high-quality grid. The ensuing mesh is formed primarily of unstructured hexahedral cells with trimmed cells adjacent to the surface. Mesh refinement is performed around the hull and the free surface. The refined mesh density in these zones is achieved using volumetric controls applied to these areas. Fig. 5 depicts a general view of the grid in the background and overset regions.

To accurately reproduce the waves, the free surface mesh is generated based on the guidelines for ship CFD applications of ITTC (2011). According to these recommendations, a minimum of 80 cells per wavelength on the free surface is necessary. In this study, each wave simulation case is conducted with a specified mesh scheme. A number of 146 cells per wavelength is used on the free surface for the case of $\lambda/L = 1.0$; and 88–292 cell layers are provided for wave length ranging from $\lambda/L = 0.6$ to 2.0 proportionally. A minimum of 16 cells are used in the vertical direction where the free surface is expected. A prism layer is used to generate the boundary layer grid and control its thickness around the no-slip body surface. A boundary layer mesh of 8 layers near the hull is used (wall $y+$ value lies in 30–60). Fig. 6 shows the refined grid near the free surface and hull body with the presence of wave for the case of $\lambda/L = 1.0$. Fig. 7 shows the side view of surface mesh on the ship hull and the local enlarged details at stern and bow areas.

Fig. 8 displays a local view of the refined mesh area around the free surface for a fifth-order Stokes regular wave with wave length $\lambda/L = 1.0$ and wave height 120 mm without the presence of ship. The figure corresponds to the xoz vertical

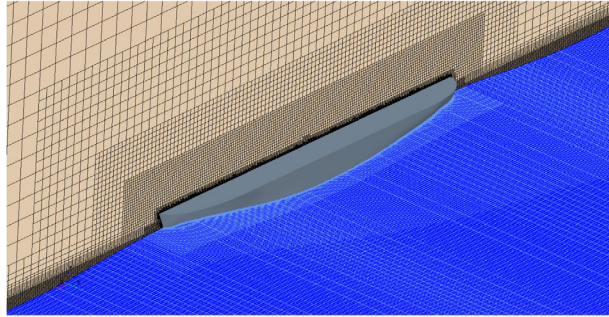


Fig. 6. Refined grid near the free surface and hull body.

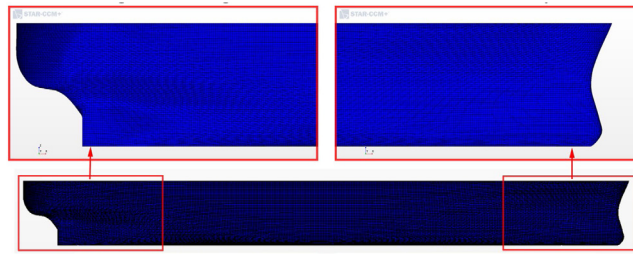


Fig. 7. Surface mesh generated on the ship hull.

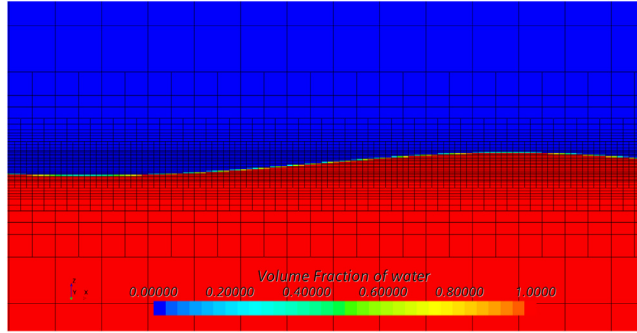


Fig. 8. A cross-section of the refined mesh area around the free surface waves.

cross-section (the longitudinal centerline plane $y = 0$). The color bar illustrates the fraction of fluid in each cell. The value of 1 and 0 represents the cell is filled with water and air, respectively. The value of 0.5 represents the cell is filled with 50% water and 50% air.

2.2.3. Wave simulation

Accurate simulation of the incident waves is fundamental for the investigation of wave-induced ship responses. Fifth-order Stokes wave, which is closer to a real nonlinear wave compared with linear Airy wave, is used in this study. In order to prevent wave decaying during its propagation and wave reflection from the boundaries, the EOM is applied to the solution by replacing the source term in the conservation equation. The EOM method was first used to solve the Navier–Stokes equations in the near-field by FEM-based and FVM-based CFD simulations by Kim et al. (2004, 2011, 2012)). It turned out to be effective and reliable in wave simulation and addressed well the wave reflection and absorbing problems (Zhang et al., 2021).

As seen in Fig. 9, the computational fluid domain is divided into two kinds of regions, which are the inner domain and outer region. The outer domain is defined from the wave inlet or outlet boundary to the inside fluid domain with a length of $1.2L$. The momentum source term is applied to the Navier–Stokes equation at the outer region to force the current CFD solution towards the theoretical solution.

The added source term applied in the forcing zone for the solution of the transport equation is expressed as follows:

$$q(\varphi) = \gamma_0 d(x)(\varphi_0 - \varphi) \quad (1)$$

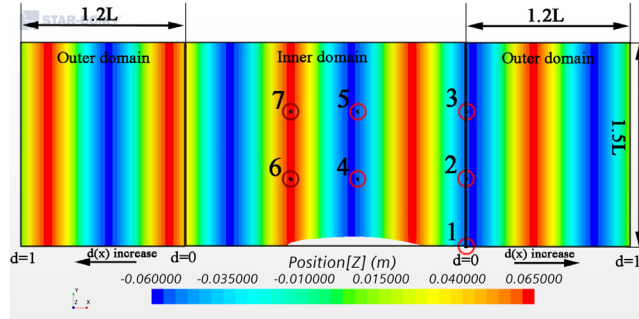


Fig. 9. Definition of wave forcing region from top view.

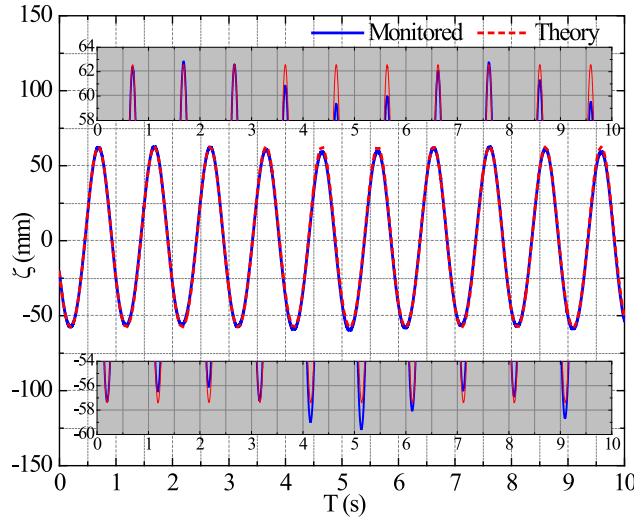


Fig. 10. Comparison of wave elevation between monitored and target value.

where γ_0 is the maximum forcing factor, $d(x)$ is distribution function of the source term over the wave forcing region, x is the distance from the inner–outer domain boundary; φ_0 and φ are the theoretical solution with the presence of target waves from Euler solver and the current solution of scalar function, respectively (Kim et al., 2012). The distribution function $d(x)$ is expressed as:

$$d(x) = \cos^2(\pi x^*/2) \quad (2)$$

where $x^* = x/d_0$ is the non-dimensional relative distance, d_0 is the length of gradient region (the distance from the inner–outer domain boundary to the outer boundary, $1.2L$ in this study).

To monitor the simulated incident waves and ship generated waves, an array of seven wave probes are arranged around the ship. The locations of these wave probes are G1 ($1.3L, 0$), G2 ($1.3L, 0.5L$), G3 ($1.3L, L$), G4 ($0.5L, 0.5L$), G5 ($0.5L, L$), G6 ($0, 0.5L$) and G7 ($0, L$), which are presented by red circles in Fig. 9. It is noted that the wave probe measured free surface elevation includes the effects of radiation wave, diffraction wave and steady wave-making caused by the advancing ship. An example of the comparison of the wave elevation in Case 4 ($\lambda/L = 1.0$, see Table 3) between monitored and target value at G1 where the influence of ship is ignorable is shown in Fig. 10. The results indicate that the incident waves are well reproduced by the EOM-based wave-making method and the error is below 2%. It is noted that the incident wave signals correspond to the encounter wave rather than in situ monitored natural wave.

2.3. Structural solver

The rigid body motions and structural deformations of the ship hull are calculated by a FEA solver with the help of ABAQUS software (Dassault Systèmes, 2014). ABAQUS is a displacement-based method and the finite element solution is based on the principle of virtual work or virtual displacement (Bathe, 2006). An implicit dynamic analysis solver is used to solve the governing equations. The time integration scheme adopted is a second-order Hilber–Hughes–Taylor (HHT) scheme, which is an extension of the Newmark- β scheme. The main features of the FEA solver and the FE model of hull are described in this section.

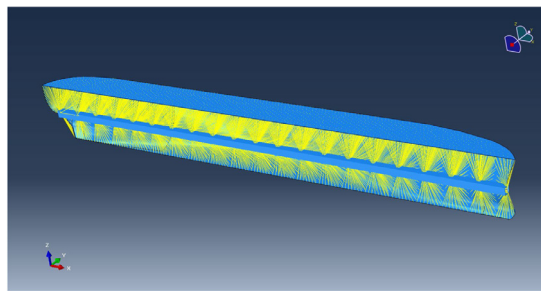


Fig. 11. Finite element mesh with beam and shell.

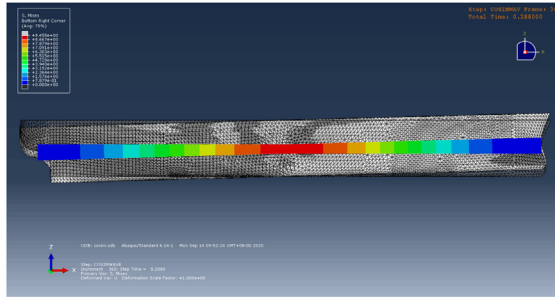


Fig. 12. Example of rigid body motions and structural deformations simulated by ABAQUS.

2.3.1. Structural model

To be in accordance with the hydrodynamic model in the CFD solver, the FEA computations are also conducted in model scale. It is assumed that the model response is symmetrical about the middle longitudinal plane when sailing in head seas. Thus only half of the model on the port side is established and a symmetry plane is used in the FEA solver. Since the fluid added mass is explicitly considered in the CFD solver through the two-way interaction method, the added mass does not need to be additionally applied to the FE model during co-simulations. The FE model of the hull comprises massless surface shell (including full main deck) and a backbone beam. The mesh discretization of the ship model for the FEA is shown in Fig. 11. The 3D shell elements (SFM3D3) that are connected to the beam nodes by kinematic coupling constraints transfer the external fluid loadings from the CFD solution to the 1D beam elements (B31) for structural dynamic analysis. The vibrational deformation of beam will also be fed back to the surface shell for the subsequent hydrodynamic analysis. The mass of hull is applied on the beam elements according to the target value shown in Fig. 3. The concentration of mass at the height of neutral axis will have some influence on the modal behavior of ship vibrations compared with real condition. However, it is known that the influence of rotary inertia of beam on the modal behavior is very small compared with mass and stiffness of beam.

The backbone beam comprises 20 elements and 21 nodes. The positions of these nodes coincide with the stations 0 to 20, which is also shown in Fig. 2. The beam has a uniform rectangular cross-section and its vertical bending stiffness ($EI = 9.88 \times 10^4 \text{ N m}^2$) was determined to meet the 2-node natural frequency of hull in vacuum. The material property of the beam elements is defined as that of steel. The hull surface mesh is created by unstructured grid consisting of 10,357 elements and 5348 nodes. The dimension of the shell elements is about 50 mm. The shell elements are divided into 21 groups and they are rigidly fixed on the corresponding nodes of beam by kinematic coupling constraints. The sectional force and moment at center of each segment beam, i.e. between adjacent nodes, are monitored.

2.3.2. Constraints and loadings

The FE model is constrained for y -axis (no sway) translation and rotations about the x -axis and z -axis (no roll and yaw) by imposing constraints on the beam nodes. Moreover, the FE model should also be restricted in the direction of x -axis to prevent longitudinal drift caused by the waves (Lakshmyarayana and Temarel, 2020). The forward speed of the ship in the co-simulation is realized by assigning an opposite speed of propagation to the waves in CFD simulations. In the FEA solver, gravity acceleration is applied to the FE model in the whole solution period since the hydrodynamic forces from the CFD are given considering the acceleration of gravity. Fig. 12 shows an example of rigid body motions and structural deformations of the ship at one certain moment with respect to the static mean position obtained by the FEA solver. In the figure the color bar denotes structural stress distributed on the beam.

Table 2
Natural frequency of model vertical bending modes.

Order	Mode	Dry condition (Hz)	Wet condition (Hz)
1st	2-node	10.154	8.856
2nd	3-node	26.241	22.791
3rd	4-node	49.747	43.270

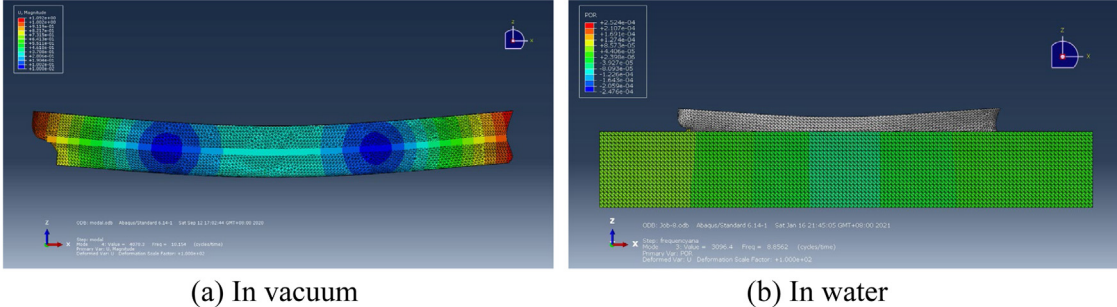


Fig. 13. Example of the 2-node modal shape of ship hull in dry and wet conditions.

2.3.3. Vertical vibration modal analysis

Prior to the co-simulations, modal analysis of the FE model hull of the S175 ship is conducted using ABAQUS to provide information about the ship model's vibrational behavior such as natural frequencies and modal shapes in both dry and wet conditions. The 2-node natural frequency of hull in dry condition is determined also to satisfy the target value by adjusting vertical bending stiffness of the backbone beam. The dry mode can be directly calculated from the eigenvalue analysis of the established FE model of hull with the help of ABAQUS.

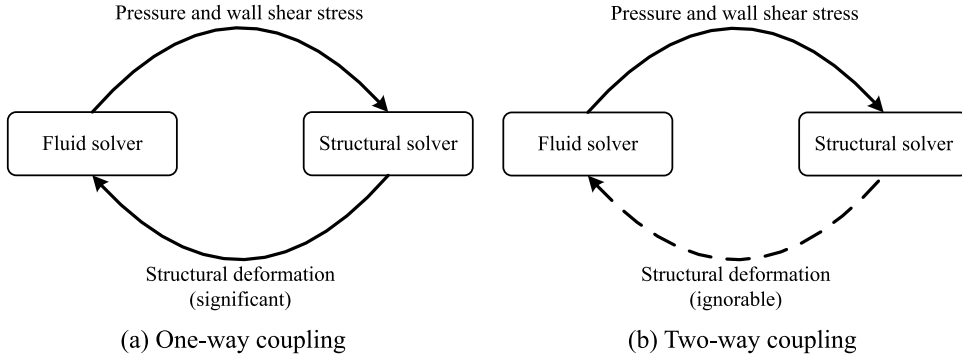
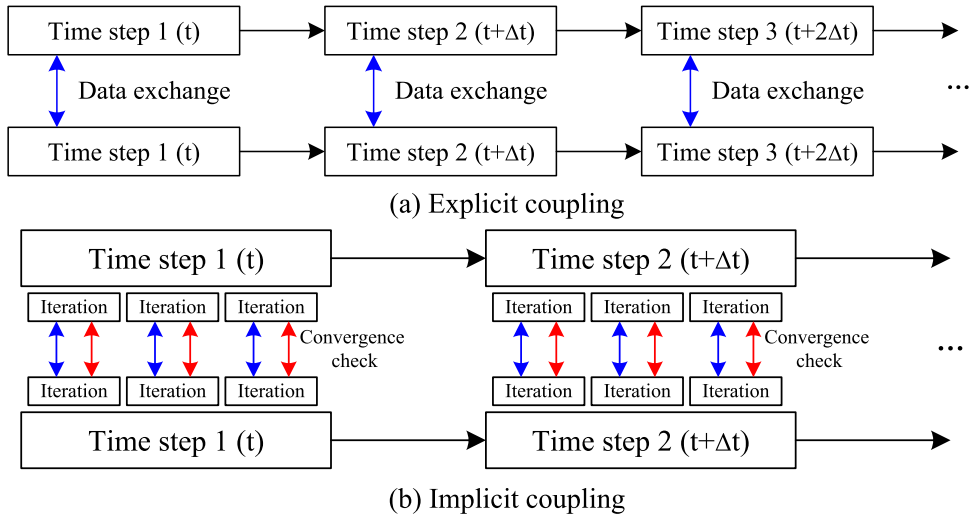
Although in two-way coupling the added mass effects due to flexible vibrations is explicitly accounted for in the CFD solver, an additional estimation of the wet mode of the hull is still useful for the confirmation and validation of the CFD-FEA co-simulated whipping frequency. Therefore, a fluid domain surrounding the hull structure is also introduced by using acoustic fluid elements (Lee et al., 2009). The density of acoustic element is 1024 kg/m³ and the bulk modulus is 2.2 GPa. A no-reflection condition is applied on the outer-surface of the basin to simulate semi-infinite extent of the water, and a total reflection condition is applied to the boundary of the water elements in the calm-water free surface. An interaction surface is generated between the fluid elements and hull body, and the inertia pressure is properly considered.

The obtained natural frequencies for the first three orders of vertical bending mode of the model both in vacuum and in water are summarized in Table 2. Fig. 13 shows example of the 2-node modal shape of the ship hull in dry and wet conditions.

2.4. Two-way coupling approach

There are generally two types of FSI co-simulation methods, which are schematized in Fig. 14. For the scheme of one-way interaction problem, the hull is considered to be rigid in the fluid domain. The fluid imposes wave loads and structural responses on the structure part while the deformation of the structure is not considered in the fluid solver. This is applicable when the influence of structural deformation on the hull loading and fluid flow is anticipated to be small as it significantly reduces computation cost. Nevertheless, in this case the two-way coupling analysis can be also conducted to obtain the structural response besides rigid body motions, even though the influence of structural deformation on the fluid field is not considered. It is noted that the fluid added mass for structural vibrations is not considered in the one-way coupling. For the other scheme of two-way interaction problem, the fluid and the structure impose a significant response on each other, i.e. the structural deformation will be accounted for in the CFD solver in turn. The added mass and its real-time variation due to change of wetted surface throughout the wave encounter period can be explicitly considered by the two-way interaction approach.

Two-way coupling can be further classified into explicit and implicit couplings. In some weak FSI problems, e.g. static deformation of a flexible hydrofoil in uniform flow, after some transient exchanges have taken place the interaction between the fluid and the structure will approach a steady-state solution, where the structural velocities finally decrease to be very small or even zero. If this is the case, an explicit coupling is preferred to calculate the transient procedure prior to the steady state is reached and the exchange of information is performed once per time step. On the other hand, when the mutual dependency on time is high between the fluid and structure solutions and a small change in one solver will have an immediate effect on the other, an implicit coupling scheme is preferred. Fig. 15 shows the framework of both explicit and implicit coupling between CFD and FEA solvers.

**Fig. 14.** Difference between one- and two-way couplings of FSI problems.**Fig. 15.** Framework of explicit and implicit couplings.

In this study, two-way interaction simulation between CFD and FEA is conducted by implicit coupling algorithm in an iteratively staggered coupling regime. A partitioned algorithm is used to execute the two-way coupling and information is exchanged at the interface sequentially and solved iteratively between CFD and FEA solvers. In the implicit coupling, the fluid loads and structural deformation are exchanged three times at each time step, and the number of such exchanges per time step is critical for the convergence, accuracy and computation cost of the coupled simulations. The iteration number within each time step is 12. Both the global rigid body motion and the hull flexural motion are solved in ABAQUS.

The coupling of hydrodynamic loadings from CFD and structural response from FEA is an important technique for the FSI co-simulation. Fortunately, both STAR-CCM+ and ABAQUS have built in mappers that can be used to apply the pressure loading to the FE model and feed back the nodal displacements to the CFD model. The scalar quantities of pressure and wall shear stress of each CFD mesh are stored at center of control volume cell or the face centroid of face mesh in the staggered grid. The nodal displacements of FE panels are stored at the vertices of the mesh. In the current two-way coupling method, least square interpolation method is used for face-to-face mapping and shape function interpolation is used for node-to-node mapping.

For FSI problems, the grid adaptation technique mainly includes morphing grid and overset grid. In the present co-simulation, a combination of overset grid and morphing grid is adopted for the FFSI problem. The rigid body motions, i.e. heave and pitch, of hull in waves are addressed by overset grid technique, which is highly efficient in the case of free surface flow for the body undergoes large amplitude motions in waves. On the other hand, the flexible deformation of hull is addressed by morphing grid. The nodal displacements that include both the rigid body motions and elastic distortions imported from FEA solver are used to redistribute the fluid grid vertices by generating an interpolation field throughout the fluid domain. The overset boundaries then move in response to the interpolation field created by the mesh morpher, which helps to maintain good quality mesh in the region in turn.

Table 3

Simulation conditions for comparative studies.

Case ID	Speed (F_n)	Wave height (H , mm)	Wave length (λ/L)	Wave frequency (ω , rad/s)	Encounter frequency (ω_e , rad/s)	Wave steepness (H/λ)	Note
1	0.275	120	0.6	4.842	9.150	0.0457	$\omega_h = 6.078\omega_e$
2	0.275	120	0.8	4.193	7.424	0.0343	$\omega_h = 7.491\omega_e$
3	0.275	120	0.9	3.954	6.825	0.0305	$\omega_h = 8.149\omega_e$
4	0.275	120	1.0	3.751	6.335	0.0274	$\omega_h = 8.779\omega_e$
5	0.275	120	1.1	3.576	5.926	0.0249	$\omega_h = 9.385\omega_e$
6	0.275	120	1.2	3.424	5.578	0.0229	$\omega_h = 9.971\omega_e$
7	0.275	120	1.5	3.062	4.786	0.0183	$\omega_h = 11.620\omega_e$
8	0.275	120	2.0	2.652	3.944	0.0137	$\omega_h = 14.101\omega_e$

2.5. Calculation conditions

A series of computation conditions are carried out to allow for a systematic analysis of the co-simulation results of ship seakeeping and hydroelastic responses. All the investigation conditions are for head regular waves. Typical ship speed of $F_n = 0.275$ is adopted so as to be in consistence with the value in the references for numerical validation. Typical wave height of 120 mm (full-scale 4.8 m) is adopted to obtain pronounced motion and load responses in moderate seas, which can be used for analyses of both linear response amplitude operators (RAO) of low-frequency wave loads and slamming and whipping loads. Table 3 summarizes the involved investigation conditions in this study.

Prior to the simulations of ship responses in a wide range of wave conditions, a convergence and uncertainty analysis on the influence of grid density, time step and fluid domain size on ship responses by the CFD–FEA coupled method were systematically conducted, and the results can be found in Huang et al. (2021b). The minimum grid size of 0.007 m is preferred and the total cell number in the fluid domain is around 4 millions, which differ for each wave length case. For this specific problem of ship hydroelastic analysis, the time step should be set smaller than 1/100 of the 2-node natural vibration period so that the high-frequency whipping loads can be well reproduced. A constant time step of 0.001 s is chosen for the two-way co-simulations. The co-simulations were run in parallel mode by workstations with a single node i9 9980XE processor with 18 cores, and it took about 10 days to obtain 10 s physical time histories of the ship model's responses in one case.

3. Global motions and vertical accelerations

The calculated vertical motions and accelerations of the ship at different wave lengths are systematically analyzed in this section. The numerical results of RAOs are also compared with some existing experimental and theoretical data.

3.1. Overview of the time series

A comprehensive comparison of the co-simulated time series of ship heave and pitch motions and vertical accelerations at FP in head regular waves at different wave lengths $\lambda/L = 0.6$ –2.0 is shown in Fig. 16. The results are presented in model scale. The positive sign of heave, pitch and acceleration denotes the emergence of ship, trim by bow and hyper-gravity, respectively. Low-pass filter is used to separate the wave frequency (WF) acceleration from the total acceleration. The results indicate that the ship heave and pitch motions are regular and sinusoidal shape for all the wave length cases, while the vertical acceleration comprises pronounced high-frequency (HF) components in addition to the WF components for all the cases due to hull girder hydroelastic vibrations.

It is worth mentioning that although the vertical displacement data includes both rigid body heave motion and structural elastic deformations, the higher order harmonics caused by elastic displacements do not appear in the vertical displacement of the node recorded in the co-simulation as they are ignorable small compared with the rigid body motion. However, the vertical acceleration is more sensitive to the high-order springing and whipping responses since they are the secondary derivative of heave and their amplitudes are proportional to the square of encounter frequency.

Both the crest and trough-peak values of heave, pitch and vertical acceleration in different wavelength conditions are identified from the time series, which are summarized in Table 4. It is noted that the peak values of both total and WF accelerations are separately identified and presented in the table. As seen from the results, the trough of heave is generally much greater than the crest value as the ship experienced obvious sinkage due to the forward speed and dynamic effects. The mean value of pitch is negative (as the ship experienced a trim by stern) for the cases of $\lambda/L = 0.6$ –1.2 and the mean value of pitch is positive (trim by bow) for the cases of $\lambda/L = 1.5$ –2.0, but the mean values are all very small. The mean acceleration generally increases with the increasing of wavelength. The largest heave and pitch crest or trough-peak occurs at $\lambda/L = 1.2$ which is at or near the ship-wave resonant frequency. However, the largest acceleration peak occurs at $\lambda/L = 1.1$ since the acceleration is sensitive to encounter frequency.

A comparative overview of the ship–wave interaction phenomena in different conditions is summarized in Fig. 17. The figures correspond to the ship sailing in a sagging state when the largest vertical motion or green water on deck occurs.

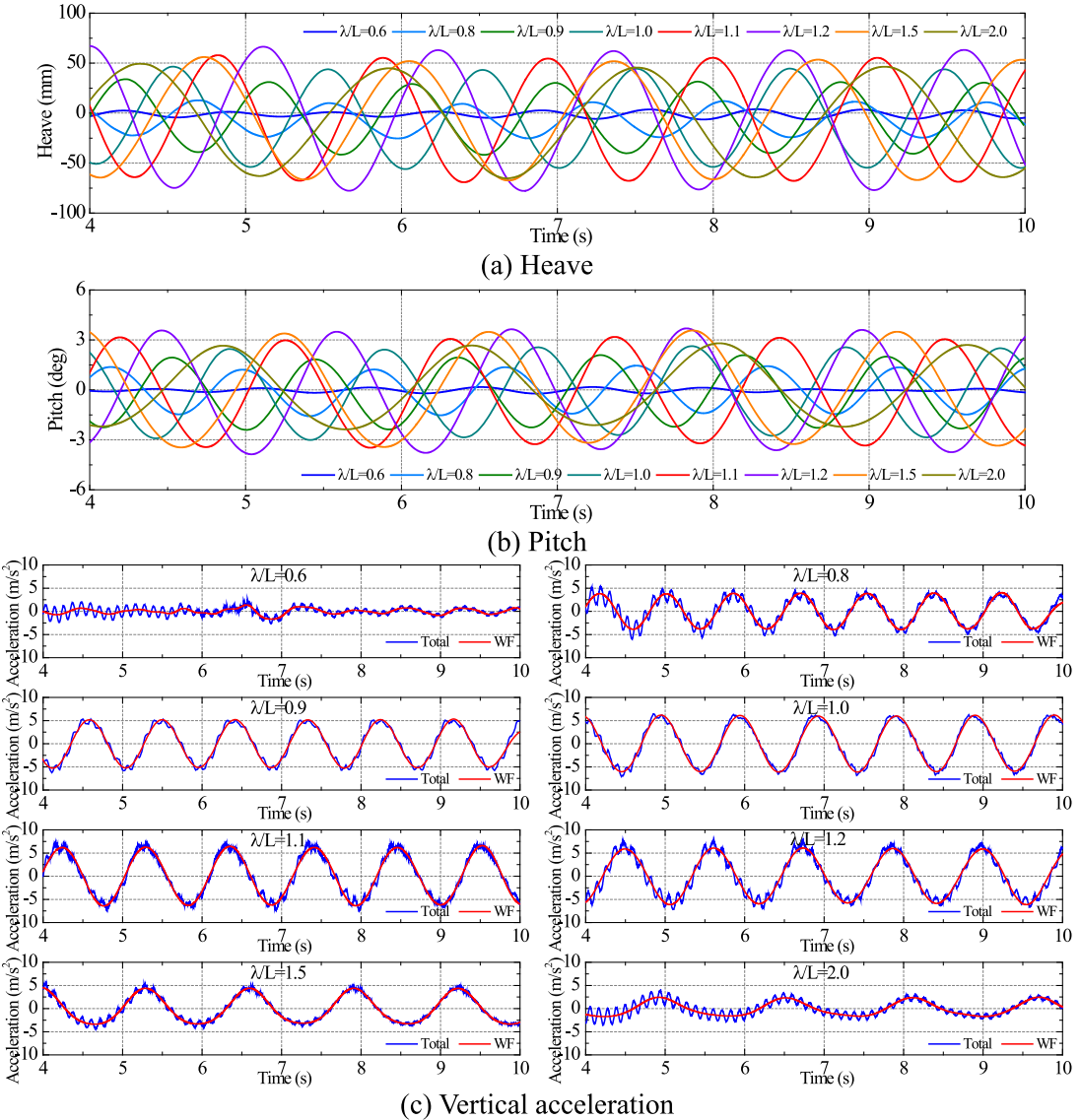


Fig. 16. Time series of motions and vertical accelerations at different wave lengths ($\lambda/L = 0.6\text{--}2.0$).

It is seen that severe green water event occurs when the ship sailed in the cases of $\lambda/L = 1.0\text{--}1.2$ due to large amplitude vertical motion. Only slight deck wetness occurs in the cases of $\lambda/L = 0.9$ and 1.5. However, severe bow flare slamming event occurs in all the cases since the wave height is relatively high. This is consistent with the fact that HF whipping acceleration occurs in all the cases as shown in Fig. 16c. Moreover, it is seen that the wake flow has been well simulated by the CFD-based VOF method.

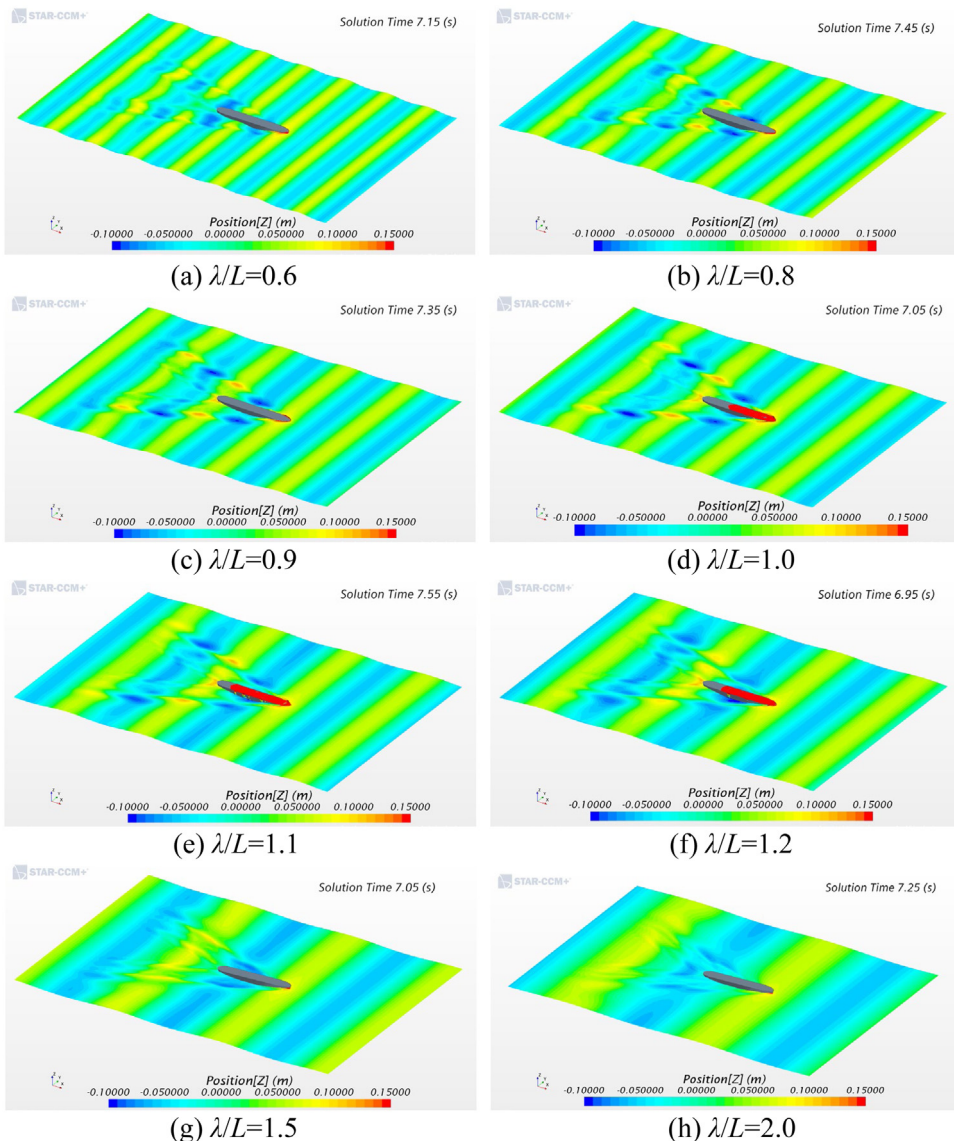
3.2. The frequency-domain spectra

The corresponding frequency-domain spectra of ship heave and pitch motions and vertical acceleration obtained by applying fast Fourier transform (FFT) on the time series data are shown in Fig. 18. The curves of heave and pitch spectra are monopeak and they have different peak frequencies and peak amplitudes for different wavelength cases. However, the vertical accelerations comprise the 1st order harmonic WF as well as 2-node, 3-node and 4-node HF components. A local enlarged view of the WF accelerations is illustrated in the insert of Fig. 18c. The peak frequencies for heave, pitch or WF acceleration in different wavelength cases are different as the wave encounter frequencies are different. However, the peak frequencies of 2-node, 3-node and 4-node HF components of vertical acceleration are identical and they are very close to the hull girder wetted natural frequencies, which are plotted by vertical dash line.

Table 4

Peak values of heave and pitch motions and vertical accelerations.

Case ID	λ/L	Heave (mm)			Pitch (deg)			Total acceleration (m/s^2)			WF acceleration (m/s^2)		
		Crest	Trough	Mean	Crest	Trough	Mean	Crest	Trough	Mean	Crest	Trough	Mean
1	0.6	4.4	-9.9	-2.8	0.102	-0.178	-0.038	1.200	-1.260	-0.030	0.690	-0.910	-0.110
2	0.8	11.6	-24.3	-6.4	1.369	-1.518	-0.074	4.300	-5.200	-0.450	3.520	-4.100	-0.290
3	0.9	31.3	-40.0	-4.4	2.091	-2.401	-0.155	5.260	-6.280	-0.510	4.870	-5.250	-0.190
4	1.0	44.2	-55.1	-5.5	2.538	-2.859	-0.160	6.490	-6.960	-0.235	6.060	-6.040	0.010
5	1.1	55.5	-68.3	-6.4	3.409	-3.507	-0.049	7.080	-7.320	-0.120	6.650	-6.120	0.265
6	1.2	64.8	-77.6	-6.4	3.610	-3.782	-0.086	7.430	-6.840	0.295	6.510	-5.510	0.500
7	1.5	53.9	-67.2	-6.7	3.576	-3.346	0.115	4.870	-4.060	0.405	4.450	-3.340	0.555
8	2.0	47.1	-64.6	-8.7	2.739	-2.235	0.252	3.430	-2.530	0.450	2.390	-1.690	0.350

**Fig. 17.** Comparison of ship motion and green water on deck.

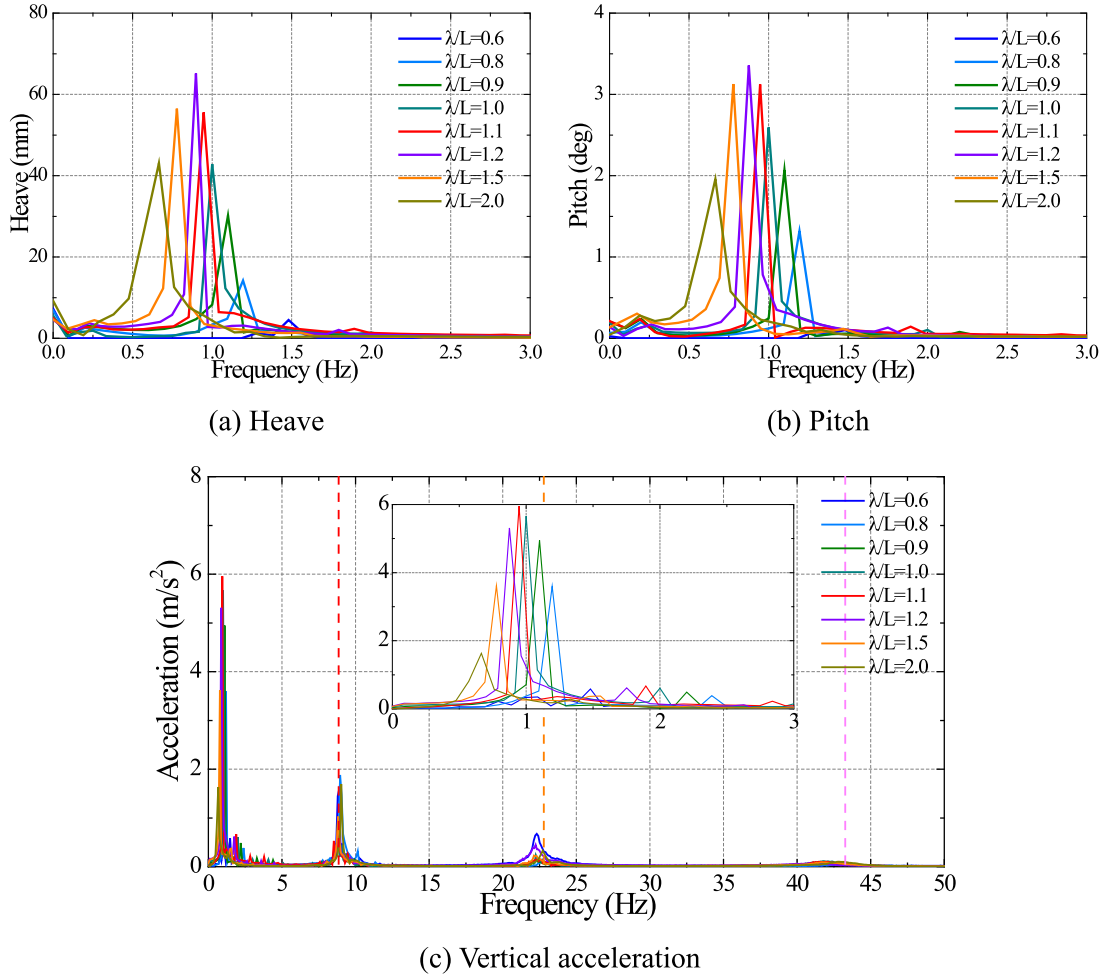
Fig. 18. Comparison of the frequency spectra ($\lambda/L = 0.6\text{--}2.0$).

Table 5
Comparison of encounter frequency with peak frequency of WF response.

Case ID	λ/L	Encounter frequency (Hz)	Heave		Pitch		Acceleration	
			Peak frequency (Hz)	Difference	Peak frequency (Hz)	Difference	Peak frequency (Hz)	Difference
1	0.6	1.457	1.481	1.65%	1.481	1.65%	1.481	1.65%
2	0.8	1.182	1.194	1.02%	1.194	1.02%	1.192	0.85%
3	0.9	1.087	1.100	1.20%	1.099	1.10%	1.100	1.20%
4	1.0	1.009	1.000	-0.89%	1.001	-0.79%	1.000	-0.89%
5	1.1	0.944	0.946	0.21%	0.946	0.21%	0.946	0.21%
6	1.2	0.888	0.898	1.13%	0.877	-1.24%	0.875	-1.46%
7	1.5	0.762	0.777	1.97%	0.777	1.97%	0.777	1.97%
8	2.0	0.628	0.664	5.73%	0.664	5.73%	0.664	5.73%

A quantitative comparison of the spectral peak frequency of heave, pitch and WF acceleration in the curves with the theoretical wave encounter frequency calculated by the following equation is summarized in Table 5.

$$\omega_e = \omega \left(1 + \frac{U\omega \cos \beta}{g} \right) \quad (3)$$

where ω_e denotes wave encounter frequency, U denotes ship speed, β denotes wave heading angle, g denotes acceleration of gravity.

The results indicate that the peak frequencies of heave, pitch and acceleration curves are identical or very close for a specific case. The difference between wave encounter frequency and peak frequency is generally small and below 2%. However, the difference is relatively large of 5.7% for the case of $\lambda/L = 2.0$. The reasons are as follows. (i) The motion

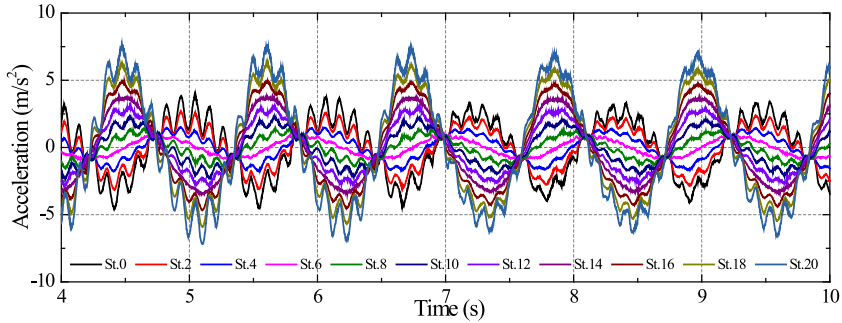


Fig. 19. Time series of vertical acceleration at different longitudinal stations ($\lambda/L = 1.2$).

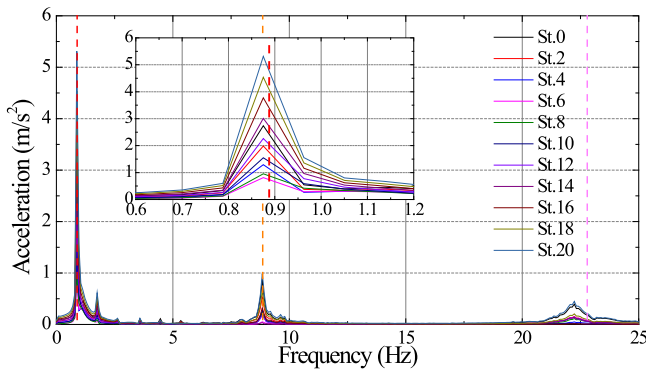


Fig. 20. Frequency spectra of vertical acceleration at different longitudinal stations ($\lambda/L = 1.2$).

response spectra are not strictly monochromatic and the energy distributes over a certain bandwidth. (ii) The fifth-order Stokes wave is used and the relevant ship response is associated with nonlinearity, which can be confirmed from the time series of vertical acceleration in the case $\lambda/L = 2.0$ in Fig. 16c. (iii) The wave reflection and shoaling effects can be more pronounced for long waves of $\lambda/L = 2.0$.

3.3. Longitudinal distribution of vertical acceleration

The vertical accelerations at each of the 21 nodes of beam element, i.e. at stations 0 to 20, have been monitored. To understand the longitudinal distribution of vertical acceleration, the time series of vertical acceleration at every two stations ranging from AP station 0 to FP station 20 in the case of $\lambda/L = 1.2$ are summarized in Fig. 19. Comparison of the related frequency spectra obtained from these time series is plotted in Fig. 20. It is observed that the time series of accelerations at different locations have different magnitude and phase, but their peak frequencies are identical for the 1st order harmonic, 2-node and 3-node whipping responses as observed from their spectra.

Moreover, the crest and trough-peak values of both total and WF accelerations at different stations are identified from the time series and they are summarized in Fig. 21. The mean peak value of both total and WF accelerations are also included in the figure. It is found that the mean peak value of both total and WF accelerations are small, but they show opposite trend. The crest and trough value curves show good symmetry behavior especially for the WF curves. The largest vertical acceleration peak (7.36 m/s^2) occurs at FP station 20. However, the lowest vertical acceleration peak (only 0.97 m/s^2) occurs at station 6 rather than at or near the midship station 10 (with peak value 2.2 m/s^2) probably due to the forward speed effects. The HF component obviously contributes to the total acceleration at the bow and stern ends, while the HF component is ignorable small at station 6.

As previously mentioned, the vertical acceleration at different longitudinal locations can be quite different. The longitudinal distribution of acceleration in different wave length conditions is seldom investigated, but this is important for many practical engineering application issues and could provide some useful guidance for such as missile launching, helicopter take-off and landing, cargo replenishment. A comparison of the longitudinal distribution of the total vertical acceleration's crest and trough-peak values in different wave length conditions is illustrated in Fig. 22, where both the original results and normalized results are presented. The results indicate that the longitudinal distribution of vertical acceleration peak show similar trends for different wave length cases and the lowest acceleration appears at station 6. The difference between accelerations at FP and AF is more pronounced for the case that near the ship-wave resonant

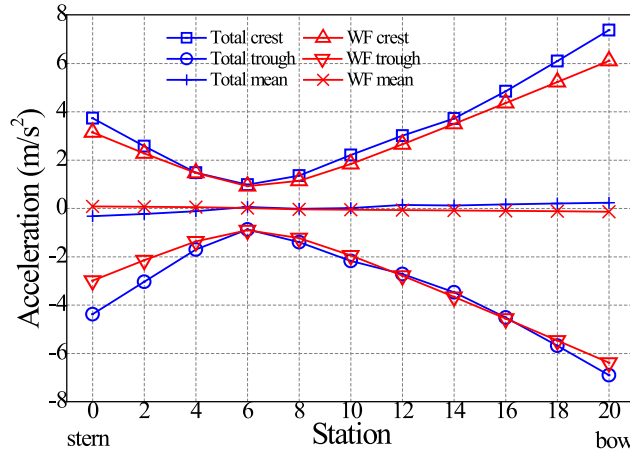


Fig. 21. Peak values of vertical acceleration at different longitudinal stations ($\lambda/L = 1.2$).

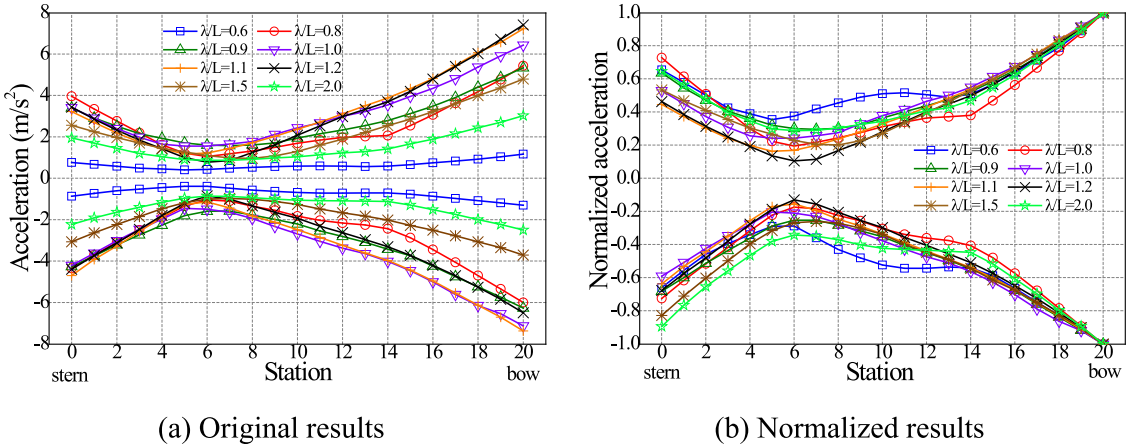


Fig. 22. Longitudinal distribution of acceleration for different wave length conditions ($\lambda/L = 0.6-2.0$).

frequency $\lambda/L = 1.2$. The tendency of curves for $\lambda/L = 0.6$ and 2.0 is slightly different from the remaining ones as the vertical responses are very small in these two cases.

3.4. Comparison of motion RAOs

The RAOs of ship motions and vertical acceleration at FP calculated by the present CFD–FEA coupling method in comparison with the theoretical and experimental data in literatures are shown in Fig. 23. The heave (z), pitch (θ) and vertical acceleration (a) are non-dimensionalized by z/ζ , $\theta/k\zeta$ and $aL/g\zeta$, respectively. Both the total and linear WF accelerations are presented for a comprehensive comparison. The numerical and experimental data used for comparison are briefly described as follows.

- The potential flow theoretical results in Lakshmynarayanan and Temarel (2020) were obtained by 2D linear frequency-domain hydroelasticity theory, which is on the basis of Timoshenko beam model and modal superposition (Bishop and Price, 1979). The 2D strip theory was used to calculate the hydrodynamic forces on the body, using Lewis sections.

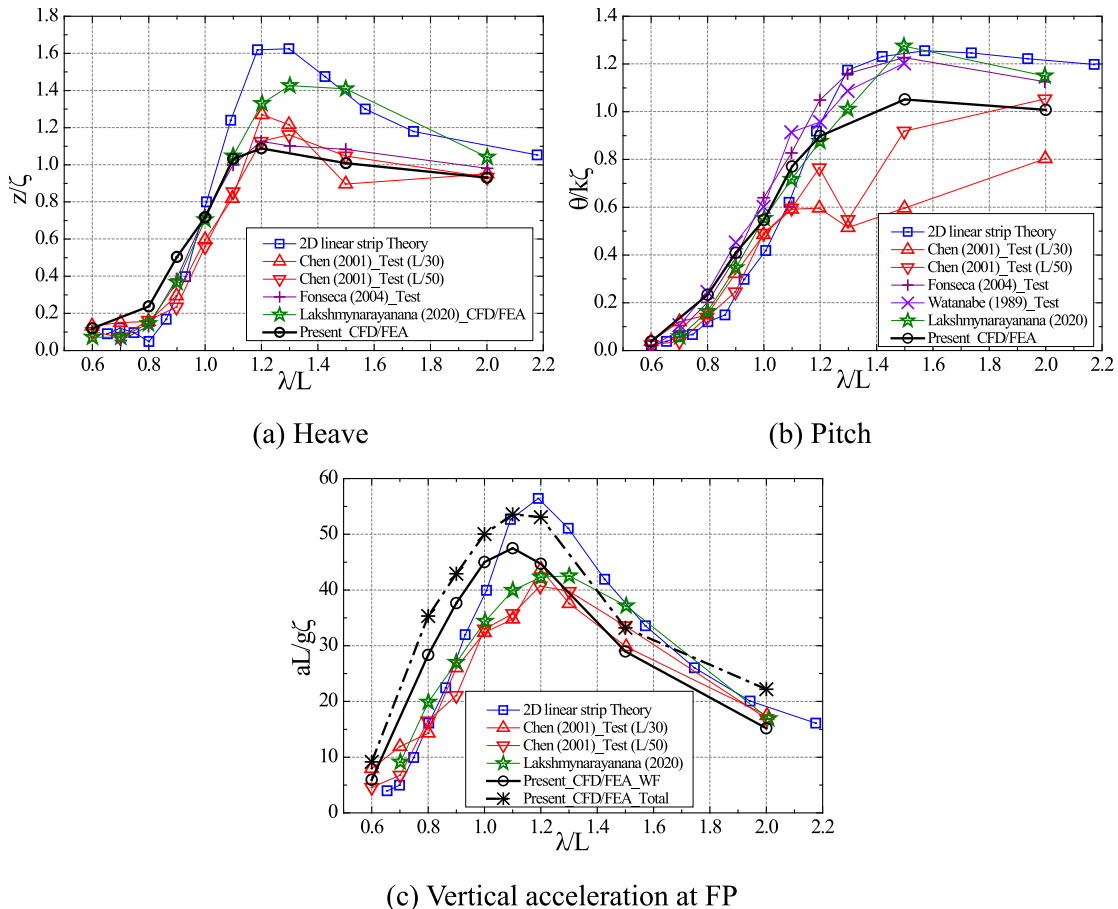
- Lakshmynarayanan and Temarel (2020) and Lakshmynarayanan and Hirdaris (2020) also used a CFD–FEA model to calculate the seakeeping and wave loads of a S175 model with a length of 3.6 m. However, their numerical setup details, such as the model scale, wave generation method, grid generation method and discretization scheme, are different from this present paper. It is worth mentioning that in their CFD code the fluid viscosity is ignored by reducing the RANS equations to the well-known Euler equations.

- Chen et al. (2001) conducted self-propelled model test of a S175 ship in the towing tank of the China Ship Scientific Research Centre (CSSRC). In their work, a fully elastic model was made up of special synthetic material ABS702 and the model has a length of 3.6 m.

Table 6

Summary of the S175 ship models in references.

Source	Type	Model length (m)	Wave height (H/L)	Forward speed (Fn)
Lakshmynarayana and Temarel (2020)	2D linear strip theory	175	N/A	0.275
Chen et al. (2001)	Tank test	3.6	1/50, 1/30	0.275
Watanabe et al. (1989)	Tank test	4.5	1/30	0.25
Fonseca and Guedes Soares (2004a,b)	Tank test	4.4	1/50	0.25
Lakshmynarayana and Temarel (2020)	CFD-FEA simulation	3.6	1/50	0.275
The present paper	CFD-FEA simulation	4.375	1/36.46	0.275

**Fig. 23.** Comparison of RAOs of motions and accelerations between different methods.

- **Watanabe et al. (1989)** measured the effects of bow flare shape on deck wetness and the VBM on a fully elastic S175 model with length 4.5 m built using synthetic resin and foam urethane. The tests were conducted in Ship Research Institute of Japan.

- **Fonseca and Guedes Soares (2004a,b)** conducted segmented model test by a 4.4 m long S175 model, which was made up of three segments connected by a rigid steel backbone at the Laboratory of Ship Dynamics of the El Pardo Model Basin in Madrid, Spain.

It is noted that although in some references (Watanabe et al., 1989; Fonseca and Guedes Soares, 2004a,b) the speed of $Fn = 0.25$ was used, many other studies (Chen et al., 2001; Lakshmynarayana and Temarel, 2020) including the present paper use $Fn = 0.275$ which is the recommended value of ITTC Procedures and Guidelines (ITTC, 2011). The influence of speed difference on the results is however not considered in this study and the RAOs are compared in a same plot. Moreover, a wave height to ship length ratio 1/50 was used by Lakshmynarayana and Temarel (2020) and Fonseca and Guedes Soares (2004a), while the value of 1/30 was used by Watanabe et al. (1989). Chen et al. (2001) used both 1/50 and 1/30 in their experiments. Table 6 summarizes the key characteristics of the experimental and numerical models involved in the comparisons.

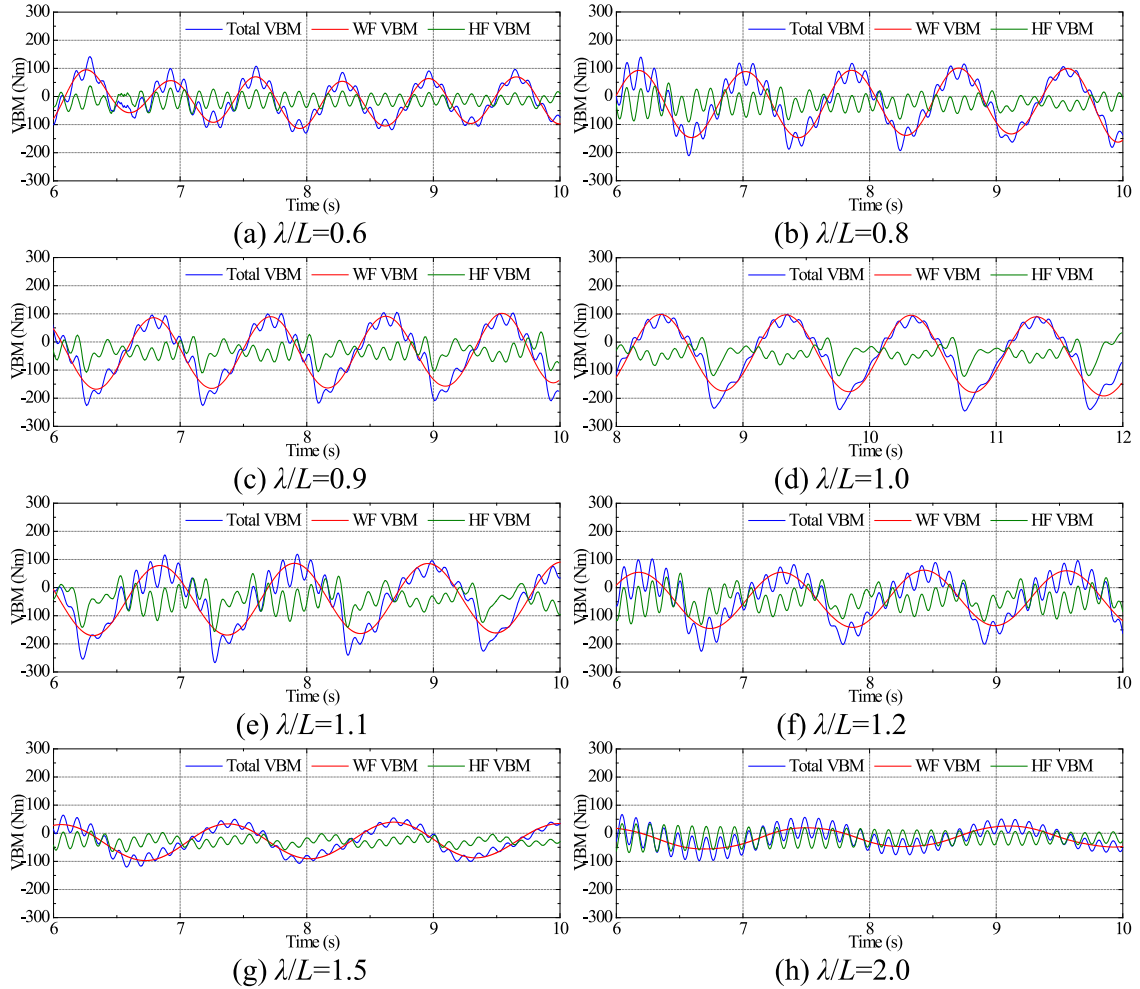


Fig. 24. Time series of VBM amidships at different wave lengths ($\lambda/L = 0.6\text{--}2.0$).

The results indicate that large scatter can be seen from the data by different approaches although the curves show same tendency. The present heave RAO shows good agreement with the experimental data by Chen et al. (2001) and Fonseca and Guedes Soares (2004a), while the 2D hydroelasticity theory and the CFD-FEA co-simulation results in Lakshmynarayananan and Temarel (2020) overestimate the heave for the cases of $\lambda/L > 1.1$. The pitch RAOs by different methods show agreement among each other in tendency for the cases of $\lambda/L < 1.1$, but the RAO curves are distinguished for longer wave length cases. To be similar with the heave RAOs, the present pitch RAO is lower than the 2D hydroelasticity theory and the CFD-FEA co-simulation results in Lakshmynarayananan and Temarel (2020) for the cases of $\lambda/L > 1.2$. However, the experimental data by Chen et al. (2001) largely underestimates the pitch compared with others for the cases of $\lambda/L > 1.2$. The RAO curves of accelerations show good agreement among each other in tendency, but the present method's result is generally higher than the reference data for the cases of $\lambda/L < 1.0$. The present resonance peak of acceleration curve, where ship-wave matching frequency occurs, is on the left of other curves.

4. Wave-induced vertical bending moments

4.1. Overview of the time series

The calculated time series of vertical bending moment (VBM) at amidships Section #10 in different conditions are summarized in Fig. 24. The positive and negative of VBM denotes hogging and sagging loads, respectively. It is noted that the calm water VBM has already been subtracted from the raw VBM data to obtain the wave-induced VBM. Bandwidth pass filtering (on the basis of FFT and inverse FFT) technique was applied to divide the total VBM into two parts of WF component (1st order harmonic wave loads) and HF components (includes 2nd and higher order harmonic springing loads and 2-node and higher order whipping loads), which are also shown along with the total VBM in each of the figures.

The results indicate that the WF VBM are in good accordance with the standard sinusoidal signal in shape, while the HF VBM generally shows irregularity due to the superposition of multi-chromatic components including springing and whipping loads. Asymmetry in hogging and sagging of WF VBM is obvious and the sagging VBM is much greater than the corresponding hogging VBM. It is worth mentioning that in this study the structural damping ratio was set at zero in order to obtain a more obvious HF vibration phenomenon of springing and whipping. Thus, the HF VBM are obviously reproduced in all the cases even for $\lambda/L = 0.6$ and 2.0.

4.2. The frequency-domain spectra

The corresponding frequency-domain spectra of VBM amidships in different wave length conditions are shown in Fig. 25. The theoretical wave encounter frequency obtained by Eq. (3) and the 2-node and 3-node natural frequencies by eigenvalue analysis of FE model in wet condition are shown in the figures for reference.

The peak frequency of the 1st order harmonic loads, i.e. WF VBM, generally coincides well with the theoretical wave encounter frequency for all the cases. The peak frequency of 2-node whipping loads generally coincides well with the 2-node wetted natural frequency apart from the case of $\lambda/L = 2.0$, where the peak frequency of 2-node whipping loads is a little higher. The same phenomenon was also found in the experiments of a catamaran model in Lavroff et al. (2013), where the high forward speed increase 2% of the 2-node whipping frequency of the catamaran compared with at zero speed. The 3-node whipping loads are not very clearly identified from the figures since the midship section is at or near the vibrational node of 3-node natural vibration mode. The 3-node and even 4-node whipping loads are however successfully reproduced at other longitudinal locations of the hull, which is reported in Section 4.3.

In addition to the 2-node whipping responses, high-order harmonic loads caused by springing responses can be also observed from these VBM spectra. The relationship between the wave encounter frequency and the 2-node wetted natural frequency is given in Table 3. It is known that the springing responses strictly occurs when the hull girder natural frequency is multiples of the encounter frequency (Lee et al., 2011b; Hong and Kim, 2014; Wang et al., 2016a,b). However, the first several high-order harmonic loads occur in the cases of $\lambda/L = 0.8$, 1.0 and 1.1 even though the 2-node natural frequency is not multiples of the encounter frequency. The reason may be threefold: (i) The high-order harmonic loads can be induced not only by springing responses but also by slamming-induced whipping responses. This is especially evident in the cases of $\lambda/L = 1.0$ and 1.1. That is the reason why the springing phenomenon is usually investigated without the presence of slamming and whipping. (ii) The 3-node or higher order hull girder natural frequency may be multiples of the encounter frequency in these cases. (iii) The actual encounter frequency or whipping frequency may slightly departure from the theoretical values due to forward speed effect, wave simulation uncertainty and numerical errors, which may result in a quite different ratio of ω_n/ω_e . Nevertheless, the high-order harmonic loads are more obvious for the case of multiples condition. For example, up to 12th order harmonic loads are clearly observed in the case of $\lambda/L = 1.2$ as the 10th order harmonic frequency is very close to the 2-node whipping frequency ($\omega_n = 9.971\omega_e$, see Table 3).

4.3. Longitudinal distribution of VBM

It is always expected to know the longitudinal distribution of VBM, which is of great importance for hull girder global structural strength assessment. As aforementioned in Section 2.1, sectional loads at each sections ranging from #1 to #20 are monitored. Fig. 26 shows the time series of VBM components at every two sections ranging from section #2 to section #20 in the case of $\lambda/L = 1.2$. In the figures, both WF and HF components obtained by filtering are presented. The scale of ordinate is set to be the same for the figures to aid comparison. Local enlarged views are also provided in some figures when the response is too small for observation. The results indicate that there exist pronounced HF components at all the sections along ship. The HF loads is comparatively large as the WF loads and it is even several times larger than the WF loads at bow sections where slamming occurs and the whipping loads is dominant.

The relevant frequency spectra of the VBM at different sections are summarized in Fig. 27. It is seen that the peak values for a specific load component are identical among the curves for different longitudinal sections. The 1st order harmonic wave encounter frequency and 2-node whipping frequency show good agreement between target and calculated, but an obvious difference can be found for the 3-node whipping frequency. To be different from the vertical acceleration spectra in Fig. 20, the high order harmonic springing loads are very pronounced in the VBM spectra.

The hogging and sagging peak values of both total and WF VBM at different sections in the case of $\lambda/L = 1.2$ are identified from the time series and they are summarized in Fig. 28a, where some literature data for longitudinal distribution of total VBM are also presented for comparison and validation. The VBM (M) is non-dimensionalized by $M/\rho g L^2 B \zeta$. ISSC (2000) has undertaken a comparative study on the wave loads of S175 ship using the theoretical data from several worldwide organizations. Thus, in this section some wave loads results from ISSC (2000) are also used for comparison in addition to the literature data described in Section 3.4. Fonseca and Guedes Soares (2002) also reported the VBM longitudinal distribution of S175 ship in a same condition obtained by both tank model experiment and 2D strip seakeeping theory. Moreover, as shown in Fig. 28b, the design loads of VBM by the new Longitudinal Strength Standard for Container Ships URS11 A issued by the International Association of Classification Societies (IACS, 2015) is also used to

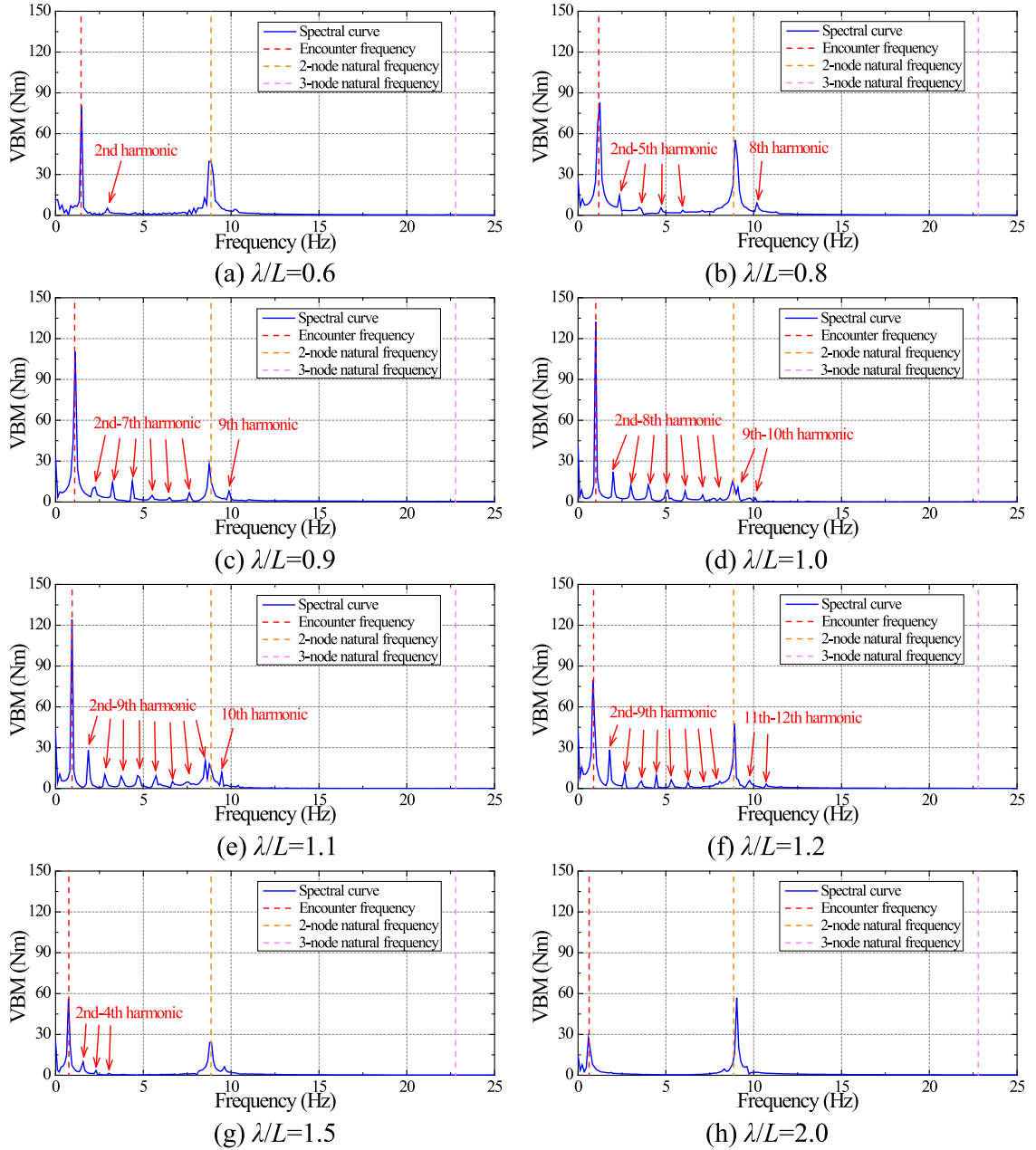


Fig. 25. Spectra of VBM amidships at different wave lengths ($\lambda/L = 0.6\text{--}2.0$).

compare with the calculated total VBM. It is worth mentioning that the following formula (BV, 2017) is used to obtain the design wave height (value of 7.07 m) to further non-dimensionalize the design loads of VBM.

$$H = 8.13 - \left(\frac{250 - 0.7L}{125} \right)^3 \quad (4)$$

It is found from Fig. 28a that the non-dimensional results by different methods generally agree well among each other even though their incident wave heights (includes $L/30$, $L/36$, $L/50$) and forward speeds (includes $Fn = 0.25$ and 0.275) are different for some cases. The hogging and sagging curves show significant asymmetry behavior. The largest hogging VBM occurs at section #10, which is near the midship section. However, the largest sagging VBM occurs at sections #11. The trough-peak of the total sagging VBM curve appears in front of the crest peak of total hogging VBM curve since the bow slamming-induced whipping effects contributes more to the total sagging VBM than hogging VBM. However, the

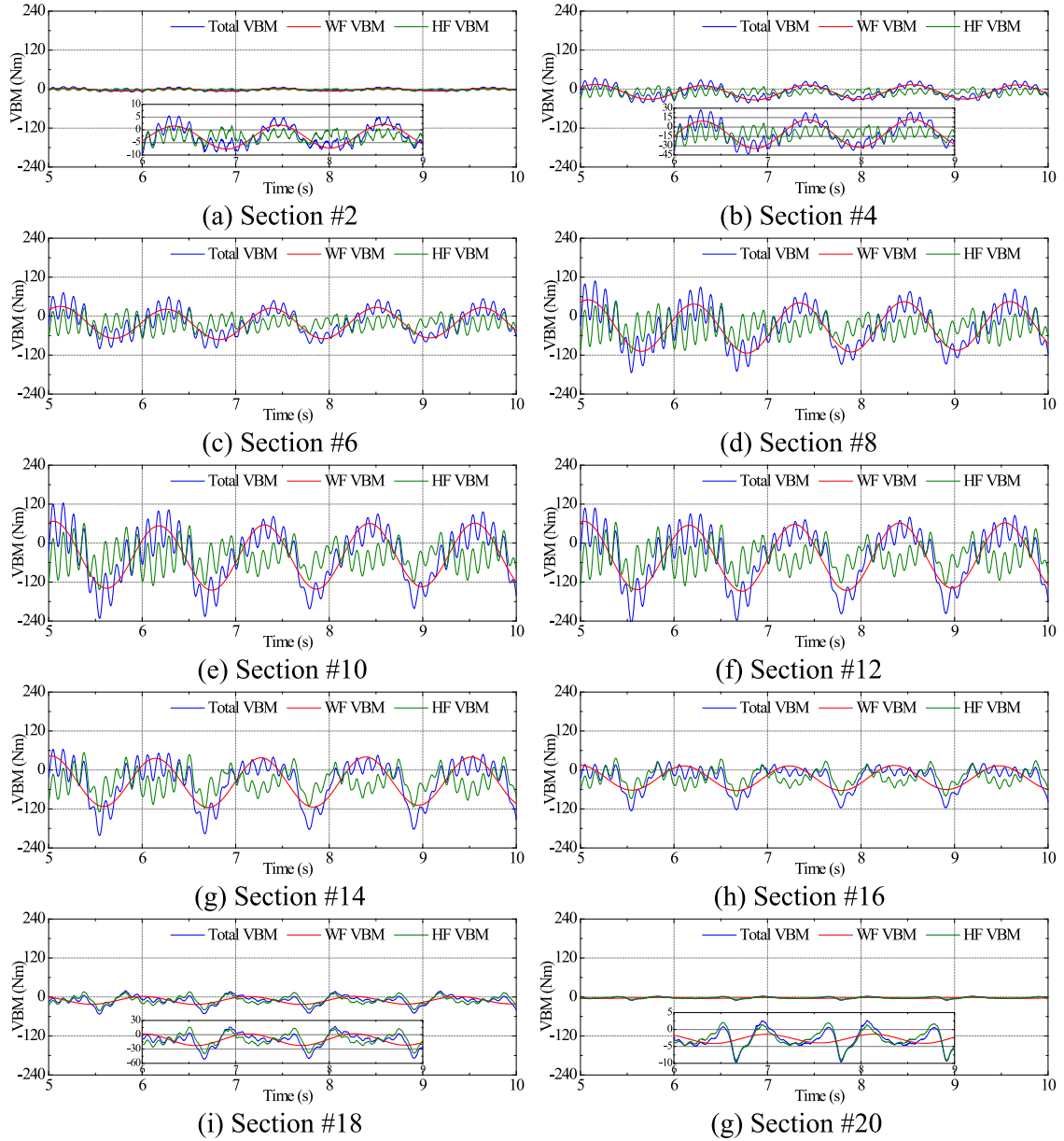


Fig. 26. Time series of VBM components at different longitudinal stations ($\lambda/L = 1.2$).

URS11 A requirement overestimates the VBM especially the sagging loads. This is partly due to the large contribution of slamming-induced sagging VBM for ship in extreme design wave with a height of 7.07 m which is much higher than the numerical simulation wave height of 4.8 m.

Moreover, the longitudinal distribution of total VBM and WF VBM in different wave length conditions calculated by the present method is compared in Fig. 29. The results indicate that the longitudinal distribution of VBM show similar trends for different wave length cases especially for the WF VBM. However, the total sagging VBM shows strong asymmetry with respect to the corresponding hogging VBM, and the trough-peak of sagging VBM curve appears in front of the corresponding crest peak of hogging VBM curves for the cases around the ship-wave matching frequency region $\lambda/L = 0.8\text{--}1.2$ due to the contribution of nonlinear whipping loads.

4.4. Comparison of VBM RAOs

The RAOs of VBM amidships, including the 1st order harmonic (WF), 2nd order harmonic, 3rd order harmonic and 2-node whipping loads, calculated by the present CFD-FEA coupling method in comparison with the theoretical

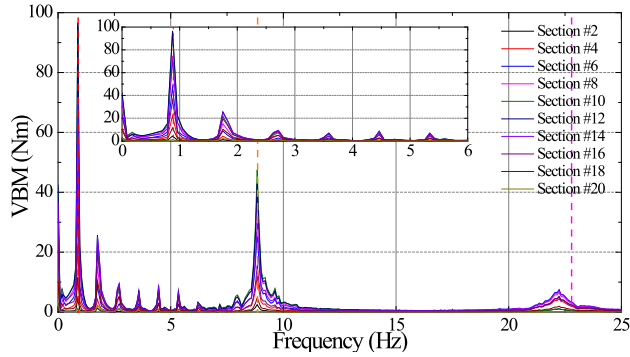


Fig. 27. Frequency spectra of VBM at different longitudinal sections ($\lambda/L = 1.2$).

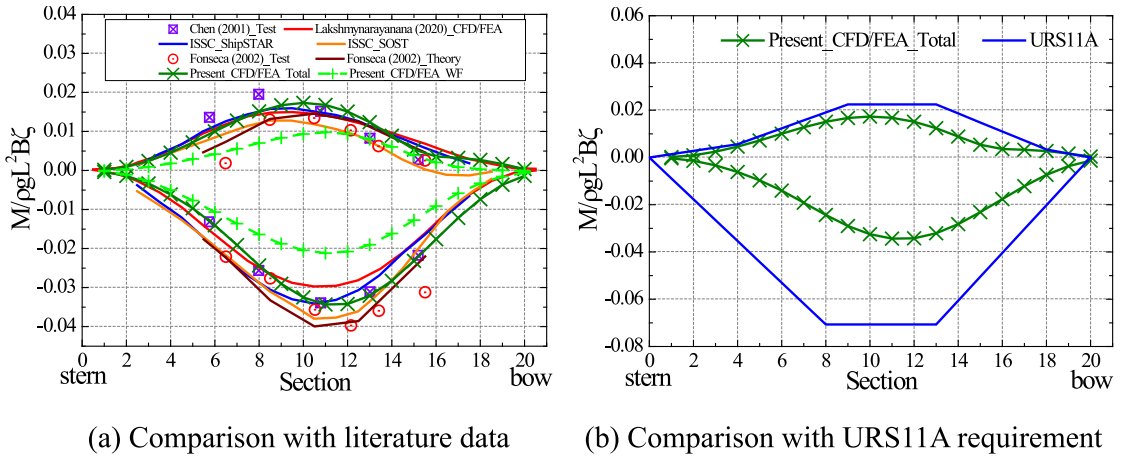


Fig. 28. Comparison of longitudinal distribution of VBM along ship ($\lambda/L = 1.2$).

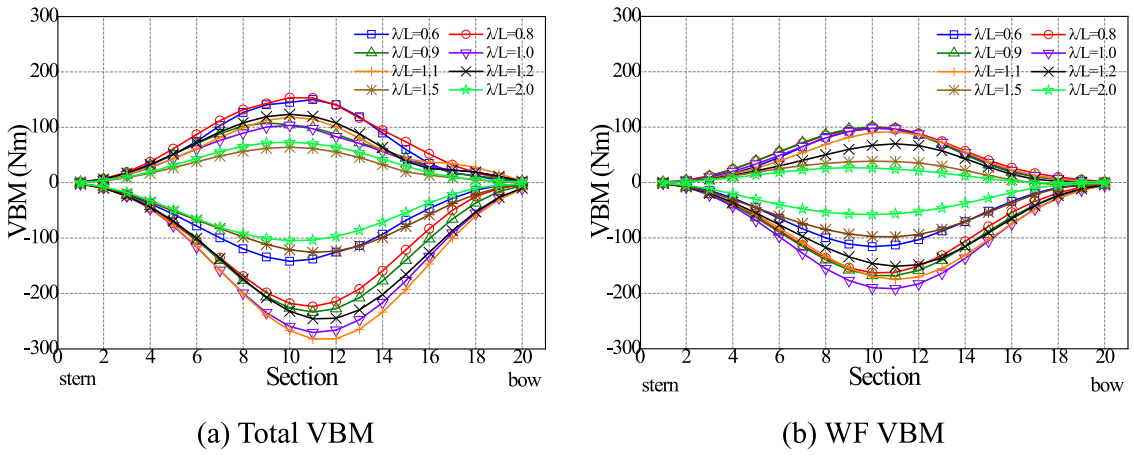


Fig. 29. Longitudinal distribution of VBM for different wave length conditions ($\lambda/L = 0.6–2.0$).

(Lakshmynarayana and Temarel, 2020; ISSC, 2000) and experimental data (Watanabe et al., 1989; Chen et al., 2001; Fonseca and Guedes Soares, 2004a) in the papers are summarized in Fig. 30. It is noted that the comparison also includes the hydroelastic responses on the S175 ship obtained by both one-way and two-way CFD-FEA coupling methods that are comparatively investigated in Lakshmynarayana and Hirdaris (2020).

As seen from Fig. 30a, the plot provides the results for both total VBM and linear WF component by the present method. The RAO curve of total VBM was obtained by non-dimensionalizing the peak-to-peak value of the time series of

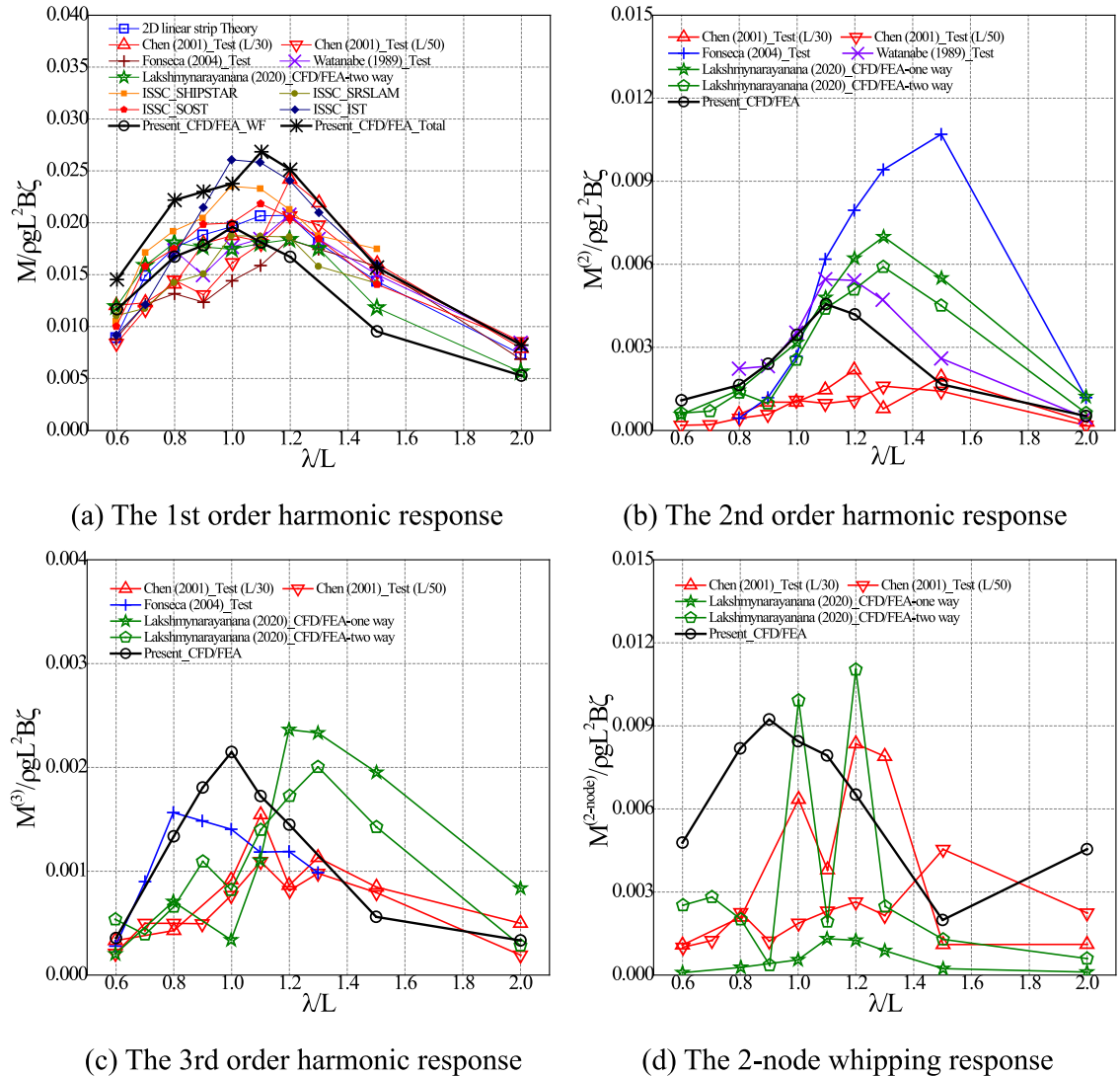


Fig. 30. Comparison of RAOs of VBM between different methods.

total VBM. The comparison indicate that the present results of WF RAO generally show good agreement with the 2D strip hydroelasticity theory, experiment by [Chen et al. \(2001\)](#) and especially the CFD–FEA co-simulation by [Lakshmynarayana and Temarel \(2020\)](#) apart from the point at $\lambda/L = 1.5$. The present method underestimates the WF VBM at $\lambda/L = 1.5$ compared with all the other results.

As seen from Fig. 30b, the present result of 2nd order harmonic loads show good agreement with the experimental data by [Watanabe et al. \(1989\)](#) who used a fully elastic monoblock model. The difference between the results by the present paper and by [Lakshmynarayana and Hirdaris \(2020\)](#) is very small for the short wave cases $\lambda/L < 1.1$, while their difference at point $\lambda/L = 1.5$ is very large. The experimental results by [Chen et al. \(2001\)](#) highly underestimate the 2nd order harmonic response of VBM, while the experimental results by [Fonseca and Guedes Soares \(2004a\)](#) largely overestimate the 2nd order harmonic response of VBM for the cases of $\lambda/L = 1.2\text{--}1.5$.

As seen from Fig. 30c, although the magnitudes of 3rd order harmonic loads by different methods are comparable, the results show large scatter especially around the peak of curve. The peak of RAO curve occurs at $\lambda/L = 1.0$ for the present result, but it occurs at $\lambda/L = 1.2\text{--}1.3$ for the result by [Lakshmynarayana and Hirdaris \(2020\)](#). The numerical results of 3rd order harmonic loads by the present paper and [Lakshmynarayana and Hirdaris \(2020\)](#) are generally greater than the experimental data in [Chen et al. \(2001\)](#) and [Fonseca and Guedes Soares \(2004a\)](#) since the structural damping is not considered in the numerical data.

As seen from Fig. 30d, the 2-node whipping results by different methods show large scatter. The peak of RAO curve occurs at $\lambda/L = 0.9$ for the present result although the values in the cases of $\lambda/L = 0.8\text{--}1.1$ are comparable. It is a bit

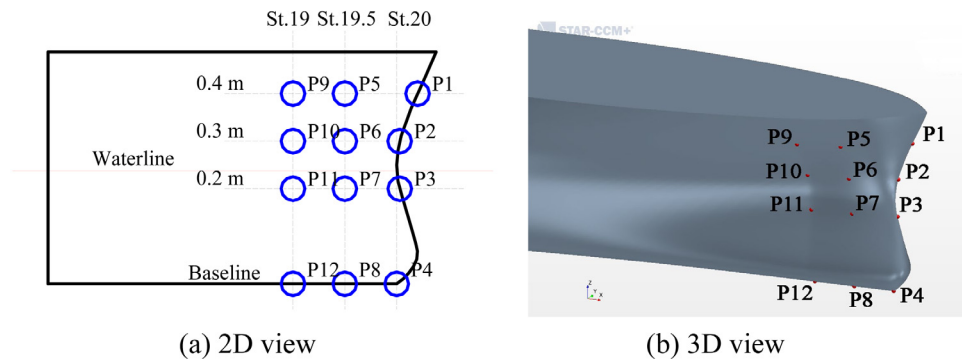


Fig. 31. Arrangement of the slamming pressure sensors.

strange that the whipping loads at $\lambda/L = 2.0$ are more pronounced than $\lambda/L = 1.5$ in the present results. There also exist large fluctuations in the values of adjacent wave length cases for the reference data. This indicates that the uncertainty and randomness for 2-node whipping loads are stronger than harmonic responses. This large scatter has also been observed in another study that deals with the hydroelastic response of another hull form (Wang et al., 2020).

As can be concluded from the analysis, the springing and whipping loads by different numerical and experimental methods can differ significantly. The main reasons are as follows: (i) Some experiments use segmented model while others use fully elastic monoblock model. (ii) The structure form of backbone beam and its property such as material and damping ratio are different for the segmented models. (iii) The number of segments of the hull is different in the numerical or experimental models. (iv) The model forward speed and wave period may fluctuate around the target values, which will have significant influence on springing loads. (v) The wave steepness and wave type are different, which will have significant influence on whipping loads.

Therefore, the related uncertainty in both numerical simulation and experiment should be further concerned especially for the prediction of whipping loads. Fortunately, in the recent years increasing efforts are being devoted to the uncertainty analysis on wave loads and whipping loads. The ISSC-ITTC Joint Committee is aimed at undertaking and promoting studies that enable the determination of the accuracy and uncertainty of existing calculation methods for comparison with experimental results and their associated uncertainty. The 5th Joint ISSC-ITTC International Workshop held in June 2021 is focused on the theme of uncertainty modeling in wave description and wave induced responses.

5. Slamming and impact pressure

The distribution behavior of wave impact pressure on the bow area for the ship sailing in different conditions is systematically investigated in this section. For the investigation of impact loads on ship when sailing in harsh waves, an array of 12 pressure sensors are arranged on the bow flare and bow bottom areas of the ship model. Fig. 31 shows the exact location of the pressure sensors on the bow surface. The gauges are positioned at the intersection of the horizontal planes (at baseline, 0.2 m, 0.3 m and 0.4 m waterline planes) with the transverse cross sections (at the station 19 and 19.5) or the middle longitudinal plane. It is noted that the pressure monitoring points are arranged on the port side or middle longitudinal plane of the hull, but in the figure they are reflected for a consistent visualization.

5.1. Time series of bow flare impact pressure

It is known that the largest bow flare impact pressures usually occur on the front of middle longitudinal plane when sailing in head waves (Hong et al., 2014; Huang et al., 2021a). The time series of impact pressure at front bow measurement points P1–3 in different wave length conditions are summarized in Fig. 32. The time series have a sampling frequency of 1000 Hz, which may not be high enough to capture the instantaneous impact peak. However, the frequency value was determined as a compromise between accuracy requirement and computational cost.

As seen from the data in Fig. 32, in most of the conditions the time series of impact pressure at one specific point is generally steady and the impact peaks for each slamming event are identical or very close. However, the peaks of P3 in $\lambda/L = 0.6$ and P1 in $\lambda/L = 0.8$ show certain scatter since these measurement points are located at alternate wet or dry conditions when the ship movement approaches to an extreme state and also due to numerical uncertainty.

The measurement point P1, which is the farthest from the waterline, did not touch the water and its pressure remains zero in the case of $\lambda/L = 0.6$ due to small vertical motions of ship in short waves. In this case, the underwater measurement point P3 was immersed in the water all the time and its amplitude of fluctuation pressure is small. Small impact pressure occurs at P1 in the cases of $\lambda/L = 0.8$ and 2.0 as the corresponding vertical motion amplitude increased compared with in $\lambda/L = 0.6$. The underwater measurement point P3 emerged from water in the cases of $\lambda/L = 0.8$ –1.5.

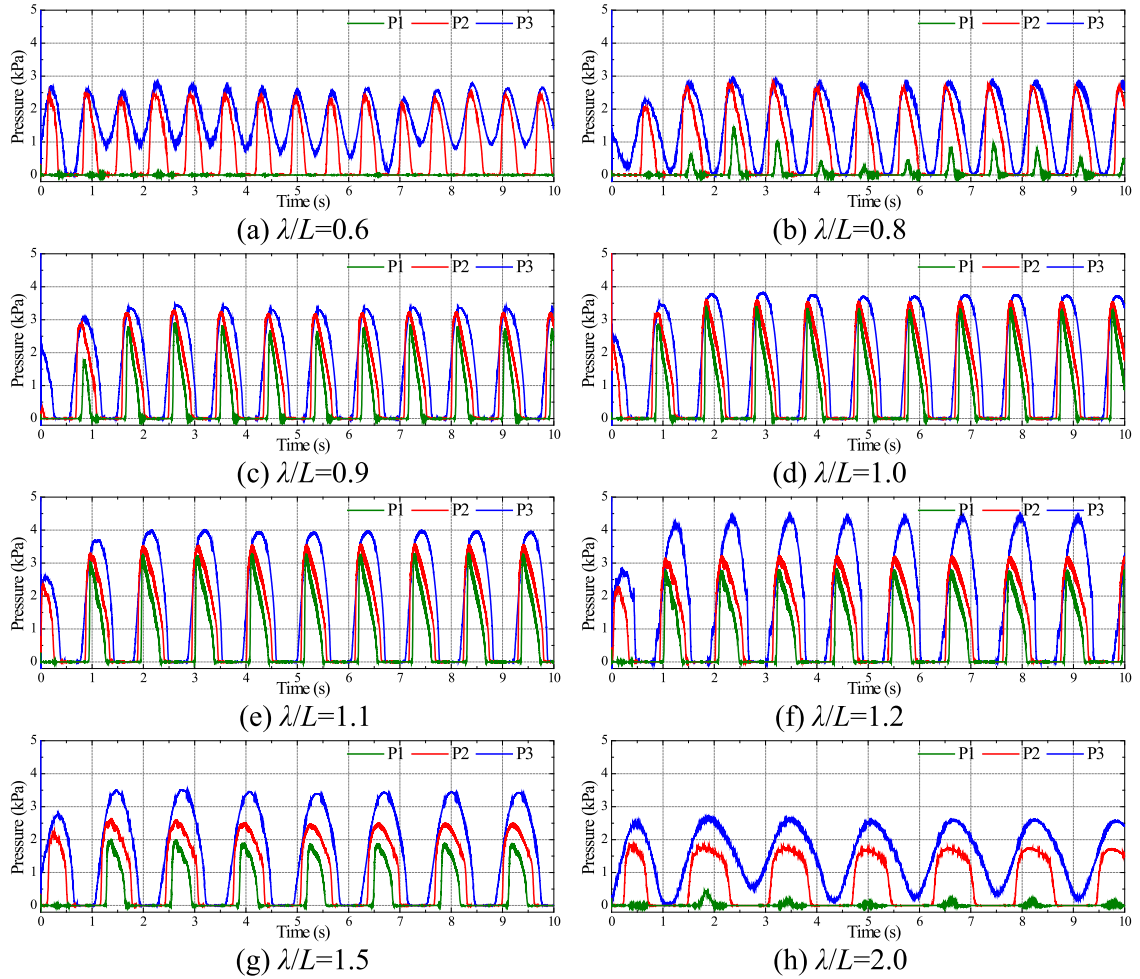


Fig. 32. Time series of impact pressure at P1–3 at different wave lengths ($\lambda/L = 0.6\text{--}2.0$).

Severe impact occurs on all point of P1–3 in the cases of $\lambda/L = 0.9\text{--}1.2$ due to large amplitude vertical motions around ship–wave matching frequency.

The largest impact peak occurs at P3 among the three points for all the cases and one possible reason is that it has an initial static pressure of 0.38 kPa. The peak pressure of P3 is respectively 1.56 kPa and 1.16 kPa greater than P1 and P2 in the case of $\lambda/L = 1.2$ due to the higher speed during water entry and water exit of P3. The peak pressure of P3 occurs at water exit phase rather than water entry phase, which can be confirmed from the blunt curve around the peak of time series and its negative dead-rise angle as shown in Fig. 31. Moreover, it is already known that the slamming peak value is governed by the relative velocity and the dead-rise angle at the point. The sharpest slamming peak occurs at P1, which has the smallest dead-rise angle. However, the peak value of P1 is generally lower than P2 in all the cases since the ship–wave vertical relative speed becomes small during water entry phase. The impact duration for each slamming event decreases from P3 to P1 in all the cases as the water contact duration decreases.

5.2. Distribution of impact pressures on bow area

Fig. 33 shows the variation of impact pressure peaks at six representative points against different wavelength cases. Fig. 33a corresponds to the measurement points P1–3 at bow flare area and Fig. 33b corresponds to the points P4, P8 and P12 at bow bottom area. The results clearly indicate that the largest bow flare impact peak occurs at P3 in the case of $\lambda/L = 1.2$. However, the largest bow bottom pressure peak occurs at P4 in the case of $\lambda/L = 1.1$. The difference of peak pressure value among P4, P8 and P12 is small at ship–wave resonant frequency range of $\lambda/L = 0.8\text{--}1.5$, while the corresponding bow flare impacts show large variation. This indicates that the nonlinearity in bow flare slamming phenomena is much stronger than bow bottom slamming.

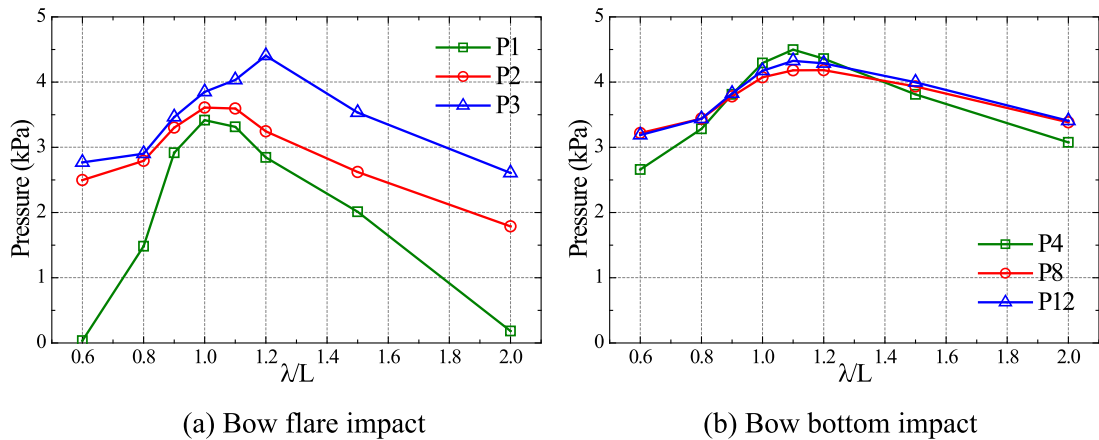
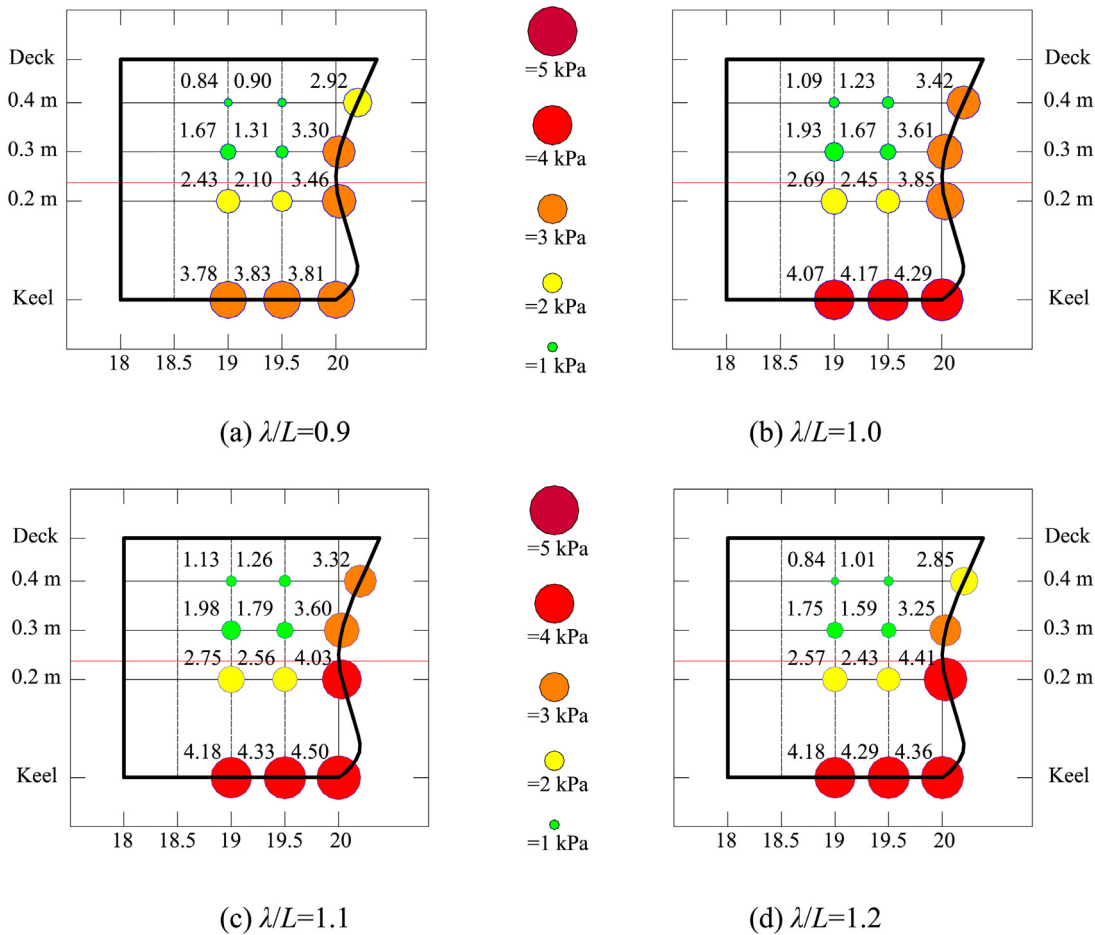
Fig. 33. Variation of impact pressure peak against wave length ($\lambda/L = 0.6\text{--}2.0$).

Fig. 34. Spatial distribution of impact pressure peak in typical conditions.

The spatial distribution of impact pressure on hull surface is a major concern for local structural design and reinforcing (Luo et al., 2012; Wang et al., 2016a,b). Fig. 34 shows the spatial distribution of impact pressure peak in four typical cases of $\lambda/L = 0.9\text{--}1.2$. In the figures, the diameter of the circle is proportional to the impact peak value. The largest impact peaks are mainly observed on the bow bottom area and one possible reason is the contribution of initial static pressure. The peak values generally decrease from the keel to the deck and also from the bow front to the backward, which shows very

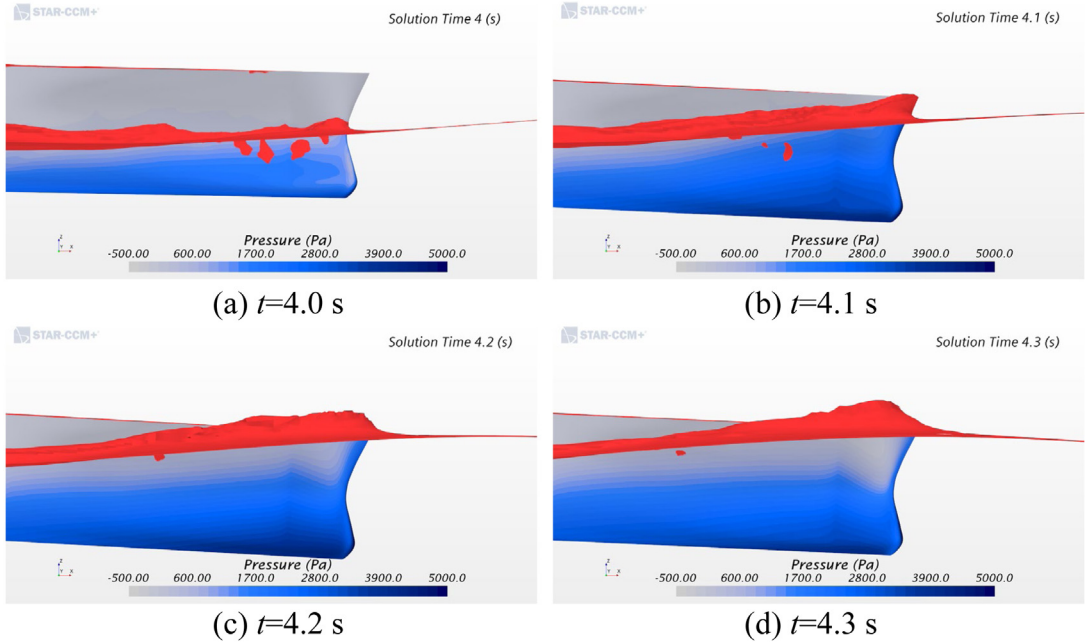


Fig. 35. Surface pressure distribution on the bow area during one slamming event ($\lambda/L = 1.1$).

similar tendency with the results by independent CFD simulation of the S175 ship's seakeeping behavior and slamming pressures in bi-directional waves (Jiao and Huang, 2020; Huang et al., 2021a).

Moreover, Fig. 35 shows the variation of surface pressure distribution on the bow area of the ship within one bow flare slamming event in the case of $\lambda/L = 1.1$. As it can be seen, there exist high pressure zone on the front and bottom bow areas, where the local structural strength should be concerned at ship design stage. Severe green water on deck occurs followed with the slamming event. Therefore, a forecastle deck is necessary for real ship to increase freeboard and prevent or reduce shipping of green water. Watanabe et al. (1989) and Fonseca and Guedes Soares (2002) have comparatively studied the motions and wave loads behavior of a modified bow with more flare and a greater volume above the waterline compared with original S175 model.

5.3. Relationship between impact pressure and global responses

The ship experienced the severest vertical motions and wave impacts in the case of $\lambda/L = 1.2$ where the ship-wave resonant responses occur. The time series of slamming pressure versus global motion and wave load responses in this condition is shown in Fig. 36. In the figure, the impact pressure at P1 is selected as a representative for slamming event identification.

As seen in Fig. 36a, the ship's pitch and heave signals are coupled all along but with opposite phase. Since slamming is induced by large amplitude motions, the motion state against impact event is analyzed first. Prior to a slamming event, the pitch and heave motions reached their mean position, where they have the maximum speed. Then the slamming event occurred when the ship bow moved down towards the wave due to trim by bow and sinkage movements. Due to the impact of bow with water, the vertical downward velocity of bow decreased rapidly. Once the bow reached the lowest position, the motion will change direction to a bow up motion due to the restoring force and moment.

Fig. 36b shows the vertical displacement and velocity of the node at FP (bow 20 station). The vertical velocity was obtained by acquiring the first-order time derivative of the displacement. The impact pressure at P2 which is mounted nearest to the FP is additionally plotted. The results indicate that the slamming event takes place when the bow moves downward from its mean position to the lowest vertical position. It confirmed that the slamming event at P2 occurred near the largest vertical velocity of this station. The time interval between the occurrence of slamming events of P1 and P2 is about 67 ms, and their vertical distance is 0.1 m. A vertical water entry velocity of 1.49 m/s for the bow station can be derived by dividing the distance with the time interval. This speed value is 0.39 m/s larger than the vertical speed of 1.10 m/s that read from the speed curve. The component speed 0.39 m/s is caused by the angular rate of pitch motion.

Fig. 36c and d shows the time series of the pressure at P1 versus VBM at bow section #18 and midship section #10, respectively. As seen from the figures, the rapid increasing whipping loads occurred after the occurrence of slamming event when the ship was in a sagging state. The whipping loads are more obvious for the VBM at bow section #18 than midship section #10. The whipping VBM decayed slowly since the structural damping is not considered in this study.

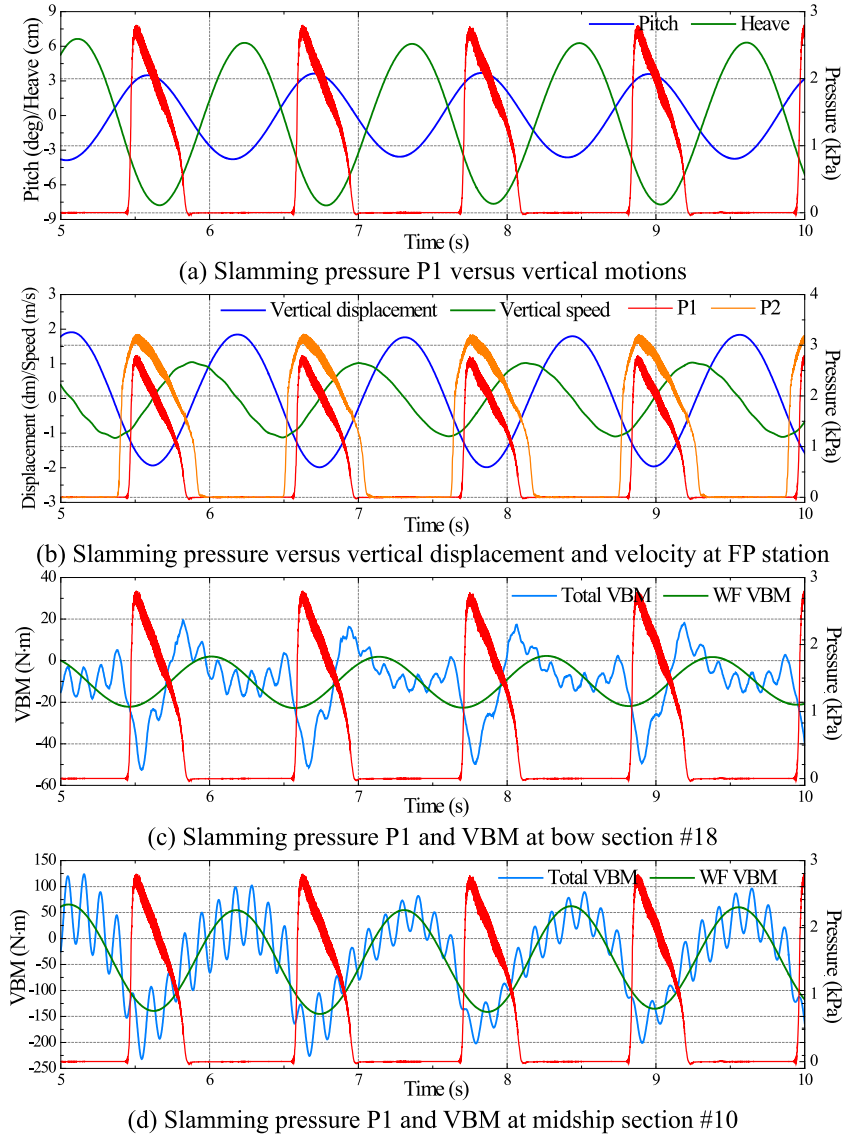


Fig. 36. Relationship between the slamming pressure at P_1 and global responses ($\lambda/L = 1.2$).

For a better understanding of the ship–wave interaction problems, physical view of the CFD simulated ship motion and the resulted slamming and green water on deck in one wave encounter period in the case of $\lambda/L = 1.2$ is shown in Fig. 37. The results indicate that there exist some amounts of green water on the deck during the whole navigational procedure. It is evident from the snapshots that the whole bow emerged into water during 6.85–7.05 s when the ship was in a sagging state. During this period, a severe slamming event occurred due to large bow down motion, which also resulted in harsh green water on deck subsequently. The graphic results also reveal that the breaking waves and violent free surface flow phenomena have been successfully captured by the CFD model.

6. Conclusions

The seakeeping and hydroelasticity including springing and whipping responses on a S175 container ship are simulated by a CFD–FEA two-way coupling FSI method. The results for ship in a relatively high sea state with different wave lengths are systematically analyzed and also compared with some existing experimental and theoretical results. The main conclusions obtained are as follows.

(1) The present FSI method is capable of predicting ship global motion and wave loads responses. The hydroelastic springing and whipping responses are well reproduced by using the two-way coupling of CFD and FEA solvers. Up to

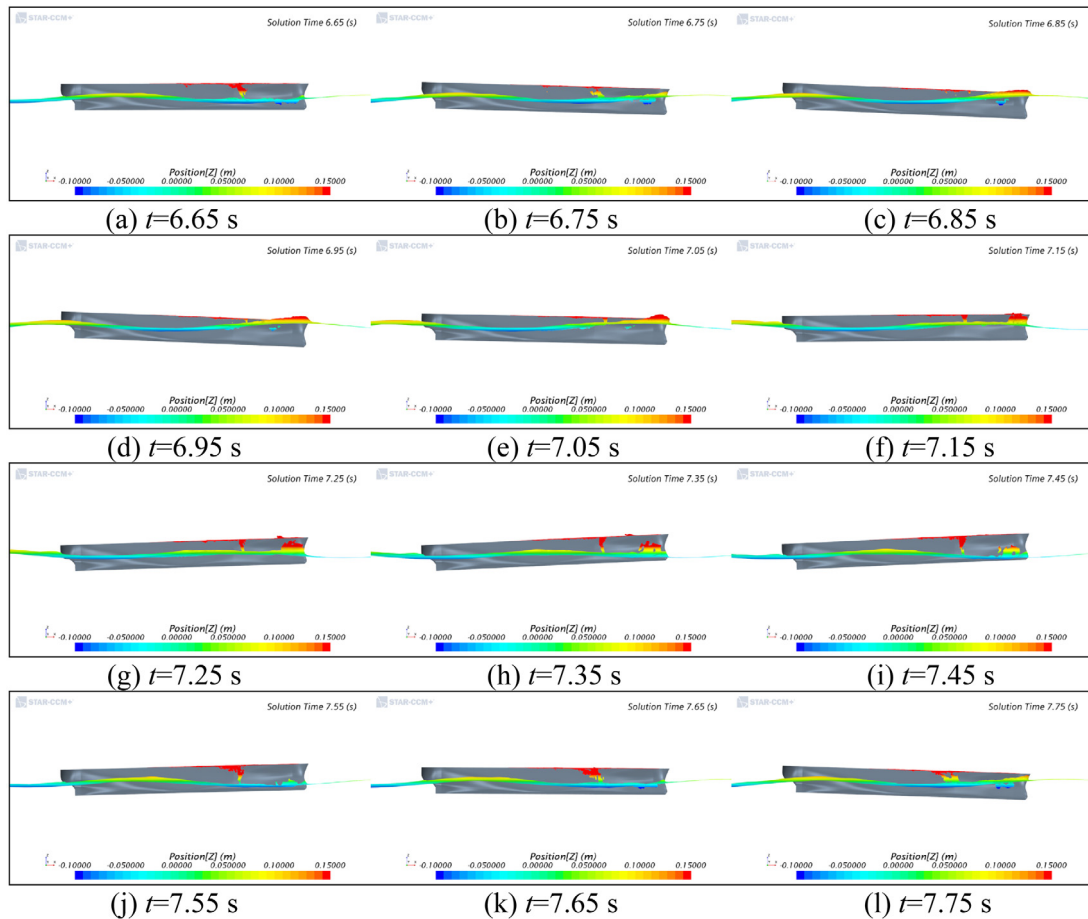


Fig. 37. Visual observation of ship vertical motions and slamming and green water on deck in one wave encounter period ($\lambda/L = 1.2$).

12th order harmonic springing and up to 4-node whipping responses have been successfully reproduced by the present FSI method.

(2) The higher order harmonics of elastic displacements do not appear in the vertical displacement recorded in the co-simulation since they are ignorable small compared with the rigid body heave motion. However, the vertical acceleration is sensitive to the whipping responses. The lowest vertical acceleration peak occurs at stern station 6 rather than midship station mainly due to the forward speed effects.

(3) The springing and whipping loads by different numerical and experimental methods can differ significantly. The uncertainty and difference in 2-node whipping loads are larger than the 1st and 2nd harmonic responses, which is probably due to the difference in structural parameters of ship models used by different institutes. Therefore, there is a real need for the structural details of typical hull forms such as S175 hull to be uniformed, provided and generalized by the scientific community of ship hydroelasticity such as ITTC and ISSC committees.

CRediT authorship contribution statement

Jialong Jiao: Methodology, Formal analysis, Visualization, Writing- original draft. **Songxing Huang:** Formal analysis, Visualization. **C. Guedes Soares:** Writing - review & editing.

Declaration of competing interest

The authors declare that they have no known competing financial interests or personal relationships that could have appeared to influence the work reported in this paper.

Acknowledgments

This research was supported by the National Natural Science Foundation of China (No. 51909096), the Guangdong Basic and Applied Basic Research Foundation (No. 2020A1515011181) and the Science and Technology Program of Guangzhou, China (No. 202102020899). This work contributes to the Strategic Research Plan of the Centre for Marine Technology and Ocean Engineering (CENTEC), which is financed by the Portuguese Foundation for Science and Technology (Fundação para a Ciência e Tecnologia — FCT) under contract UIDB/UIDP/00134/2020. The first author would also like to thank the China Scholarship Council (CSC) for the financial support of his one-year visit to CENTEC at the University of Lisbon.

Appendix A. Supplementary data

Supplementary material related to this article can be found online at <https://doi.org/10.1016/j.jfluidstructs.2021.103354>.

References

- Bakica, A., Malenica, S., Vladimir, N., 2020. Hydro-structure coupling of CFD and FEM - Quasi-static approach. *Ocean Eng.* 217, 108118.
- Bathe, K.J., 2006. Finite Element Procedures. Prentice Hall, New Jersey, USA.
- Bishop, R.E.D., Price, W.G., 1979. Hydroelasticity of Ships. Cambridge University Press.
- Bishop, R.E.D., Price, W.G., Wu, Y., 1986. A general linear hydroelasticity theory of floating structures moving in a seaway. *Phil. Trans. R. Soc. A* 316, 375–426.
- BV, 2017. Rules for the Classification of Steel Ships, Part B - Hull and Stability. NR 467.
- CD-Adapco, 2019. User Guide STAR-CCM+ Version 14.02.
- Chen, R.Z., Du, S.X., Wu, Y.S., Lin, J.R., Hu, J.J., Yue, Y.L., 2001. Experiment on extreme wave loads of a flexible ship model. In: Proceedings of the Eighth International Symposium on Practical Design of Ships and Other Floating Structures, Vol. 2. pp. 871–878. Shanghai, China, 2001 Sep 16 to 21.
- Choi, J., Yoon, S.B., 2009. Numerical simulations using momentum source wave-maker applied to RANS equation model. *Coast. Eng.* 56, 1043–1060.
- Corak, M., Parunov, J., Guedes Soares, C., 2018. Structural reliability analysis of container ships under combined wave and whipping loads. *J. Ship Res.* 62 (3), 115–133.
- Dassault Systèmes, 2014. Abaqus 6.14 Manual, Providence, RI, USA.
- Datta, R., Guedes Soares, C., 2020. Analysis of the hydroelastic effect on a container vessel using coupled BEM-FEM method in the time domain. *Ships Offshore Struct.* 15 (4), 393–402.
- Deng, R., Luo, F.Q., Wu, T.C., Chen, S.Y., Li, Y.L., 2019. Time-domain numerical research of the hydrodynamic characteristics of a trimaran in calm water and regular waves. *Ocean Eng.* 194, 106669.
- Drummen, I., Wu, M., Moan, T., 2009. Experimental and numerical study of containership responses in severe head seas. *Mar. Struct.* 22, 172–193.
- Fonseca, N., Guedes Soares, C., 2002. Comparison of numerical and experimental results of nonlinear wave-induced vertical ship motions and loads. *J. Mar. Sci. Technol.* 6, 193–204.
- Fonseca, N., Guedes Soares, C., 2004a. Experimental investigation of the nonlinear effects on the vertical motions and loads of a containership in regular waves. *J. Ship Res.* 48, 118–147.
- Fonseca, N., Guedes Soares, C., 2004b. Experimental investigation of the nonlinear effects on the statistics of vertical motions and loads of a containership in irregular waves. *J. Ship Res.* 48, 148–167.
- Gao, Z.L., Wang, Y.L., Su, Y., Chen, L., 2018. Numerical study of damaged ship's compartment sinking with air compression effect. *Ocean Eng.* 147, 68–76.
- Guo, B.J., Steen, S., Deng, G.B., 2014. Seakeeping prediction of KVLCC2 in head waves with RANS. *Appl. Ocean Res.* 35, 56–67.
- Han, F.L., Wang, C.H., Hu, A.K., 2017. Numerical investigation of wave-induced vibrations and their effect on the fatigue damage of container ships. *Ocean Eng.* 142, 245–258.
- Hashimoto, H., Yoneda, S., Omura, T., Umeda, N., Matsuda, A., Stern, F., Tahara, Y., 2020. CFD prediction of wave-induced forces on ships running in irregular stern quartering seas. *Ocean Eng.* 239, 106277.
- Hirdaris, S.E., Bai, W., Dessim, D., Ergin, A., Gu, X., Hermundstad, O.A., Huijsmans, R., Iijima, K., Nielsen, U.D., Parunov, J., Fonseca, N., Papanikolaou, A., Argyriadis, K., Incecik, A., 2014. Loads for use in the design of ships and offshore structures. *Ocean Eng.* 78, 131–174.
- Hirdaris, S.E., Temarel, P., 2009. Hydroelasticity of ships: recent advances and future trends. *Proc. Inst. Mech. Eng. M* 223, 305–330.
- Hong, S.Y., Kim, B.W., 2014. Experimental investigations of higher-order springing and whipping-WILS project. *Int. J. Nav. Archit. Ocean Eng.* 6, 1160–1181.
- Hong, S.Y., Kim, K.H., Kim, B.W., Kim, Y.S., 2014. Experimental study on the bow-flare slamming of a 10,000 TEU containership. In: Proceedings of the Twenty-fourth (2014) International Ocean and Polar Engineering Conference, Busan, Korea, June 15–20, 2014. pp. 816–823.
- Huang, H., Chen, H.C., 2020. Investigation of mooring damping effects on vortex-induced motion of a deep draft semi-submersible by coupled CFD-fem analysis. *Ocean Eng.* 210, 107418.
- Huang, S.X., Jiao, J.L., Chen, C.H., 2021a. CFD prediction of ship seakeeping behavior in bi-directional cross wave compared with in uni-directional regular wave. *Appl. Ocean Res.* 107, 102426.
- Huang, S.X., Jiao, J.L., Guedes Soares, C., 2021b. Uncertainty analysis on the CFD-FEA coupled simulations of ship wave loads and whipping responses. *Mar. Struct.* (submitted for publication).
- IACS, 2015. UR S11A, Longitudinal Strength Standard for Container Ships.
- Islam, H., Mohapatra, S.C., Gadelho, J., Guedes Soares, C., 2019. OpenFOAM analysis of the wave radiation by a box-type floating structure. *Ocean Eng.* 193, 106532.
- ISSC, 2000. Committee VI.1. Extreme hull girder loading. In: Proceedings of the 14th International Ship and Offshore Structures Congress, Vol. 2. pp. 263–320.
- ITTC Procedures and Guidelines, 2011. Practical guidelines for ship CFD applications. 7.5-03-02-03.
- Jiao, J.L., Chen, Z.Y., Chen, C.H., Ren, H.L., 2020. Time-domain hydroelastic analysis of nonlinear motions and loads on a large bow-flare ship advancing in high irregular seas. *J. Mar. Sci. Technol.* 25, 426–454.
- Jiao, J.L., Huang, S.X., 2020. CFD simulation of ship seakeeping performance and slamming loads in bi-directional cross wave. *J. Mar. Sci. Eng.* 8 (312).
- Jiao, J.L., Huang, S.X., Guedes Soares, C., 2021. Numerical simulation of ship motions in cross waves using CFD. *Ocean Eng.* 223, 108711.

- Kim, J., Jaiman, R., Cosgrove, S., O'sullivan, J., 2011. Numerical wave tank analysis of wave run-up on a truncated vertical cylinder. In: Proceedings of the ASME 2011 30th International Conference on Ocean, Offshore and Arctic Engineering. ASME, Rotterdam, The Netherlands, pp. 805–814.
- Kim, Y., Kim, K.H., Kim, Y., 2009. Springing analysis of a seagoing vessel using fully coupled BEM–FEM in the time domain. *Ocean Eng.* 36 (11), 785–796.
- Kim, J.W., Kyung, J.H., Bai, K.J., Ertekin, R.C., 2004. A numerical study of nonlinear diffraction loads on floating bodies due to extreme transient waves. In: 25th Symposium on Naval Hydrodynamics. St. John's, Newfoundland and Labrador, CANADA.
- Kim, J., O'Sullivan, J., Read, A., 2012. Ringing analysis of a vertical cylinder by Euler overlay method. In: Proceedings of the ASME 2012 31st International Conference on Ocean, Offshore and Arctic Engineering. ASME, Rio de Janeiro, Brazil, pp. 855–866.
- Lakshmynarayana, P.A.K., Hirdaris, S., 2020. Comparison of nonlinear one- and two-way FFSI methods for the prediction of the symmetric response of a containership in waves. *Ocean Eng.* 203, 107179.
- Lakshmynarayana, P.A., Temarel, P., 2020. Application of a two-way partitioned method for predicting the wave-induced loads of a flexible containership. *Appl. Ocean Res.* 96, 102052.
- Lavr off, J., Davis, M.R., Holloway, D.S., Thomas, G., 2013. Wave slamming loads on wave-piercer catamarans operating at high-speed determined by hydro-elastic segmented model experiments. *Mar. Struct.* 33, 120–142.
- Lee, D., Maki, K., Wilson, R., Troesch, A., 2009. Dynamic response of a marine vessel due to wave-induced slamming. In: Vibro-Impact Dynamics of Ocean Systems and Related Problems. In: Lecture Notes in Applied and Computational Mechanics, vol. 44, pp. 161–172.
- Lee, H., Song, M.C., Han, S., Chang, B.J., Suh, J.C., 2017. Hydro-elastic aspects of a composite marine propeller in accordance with ply lamination methods. *J. Mar. Sci. Technol.* 22, 479–493.
- Lee, Y., Wang, Z.H., White, N., Hirdaris, S.E., 2011a. Time domain analysis of springing and whipping responses acting on a large container ship. In: Proceedings of the ASME 2011 30th International Conference on Ocean, Offshore and Arctic Engineering (OMAE2011), June 19–24, 2011. Rotterdam, The Netherlands.
- Lee, Y., White, N., Wang, Z.H., Hirdaris, S.E., Zhang, S.M., 2011b. Comparison of springing and whipping responses of model tests with predicted nonlinear hydroelastic analyses. In: Proceedings of the Twenty-first International Offshore and Polar Engineering Conference Maui, Hawaii, USA, June 19–24, 2011. pp. 453–460.
- Lee, Y., White, N., Wang, Z., Hirdaris, S.E., Zhang, S., 2012. Comparison of springing and whipping responses of model tests with predicted nonlinear hydroelastic analyses. *Int. J. Offshore Pol. Eng.* 22 (3), 1–8.
- Li, H., Hao, L.Z., Chen, X.B., Ren, H.L., 2020. Frequency-domain hybrid method on motions of ship with forward speed. *Ocean Eng.* 197, 106882.
- Li, Z.F., Ren, H.L., Tong, X.W., Li, H., 2015. A precise computation method of transient free surface Green function. *Ocean Eng.* 105, 318–326.
- Liu, S.K., Papanikolaou, A.D., 2011. Time-domain hybrid method for simulating large amplitude motions of ships advancing in waves. *Int. J. Nav. Archit. Ocean Eng.* 3 (1), 72–79.
- Liu, H., Zhou, B., Han, X.S., Zhang, T., Zhou, B.K., Gho, W.M., 2020. Numerical simulation of water entry of an inclined cylinder. *Ocean Eng.* 215, 107908.
- Luo, H.B., Wang, H., Guedes Soares, C., 2012. Numerical and experimental study of hydrodynamic impact and elastic response for one free-drop wedge with stiffened panels. *Ocean Eng.* 40, 1–14.
- Ma, S.Y., Mahfuz, H., 2012. Finite element simulation of composite ship structures with fluid structure interaction. *Ocean Eng.* 52, 52–59.
- Malenica, S., Derbanne, Q., 2014. Hydro-structural issues in the design of ultra large container ships. *Int. J. Nav. Archit. Ocean Eng.* 6, 983–999.
- McVicar, J., Lavr off, J., Davis, M.R., Thomas, G., 2018. Fluid–structure interaction simulation of slam-induced bending in large high-speed wave-piercing catamarans. *J. Fluids Struct.* 82, 35–58.
- Moctar, O., Ley, J., Oberhagemann, J., Schellin, T., 2017. Nonlinear computational methods for hydroelastic effects of ships in extreme seas. *Ocean Eng.* 130, 659–673.
- Paik, K.J., Carrica, P.M., 2014. Fluid–structure interaction for an elastic structure interacting with free surface in a rolling tank. *Ocean Eng.* 84, 201–212.
- Pernod, L., Ducoin, A., Le Sourine, H., Astolfi, J.A., Casari, P., 2019. Experimental and numerical investigation of the fluid–structure interaction on a flexible composite hydrofoil under viscous flows. *Ocean Eng.* 194, 106647.
- Rajendran, S., Guedes Soares, C., 2016. Numerical investigation of the vertical response of a containership in large amplitude waves. *Ocean Eng.* 123, 440–451.
- Singh, S.P., Sen, D., 2007. A comparative study on 3D wave load and pressure computations for different level of modelling of nonlinearities. *Mar. Struct.* 20, 1–24.
- Sun, T.Z., Zhou, L., Yin, Z.H., Zong, Z., 2020. Cavitation bubble dynamics and structural loads of high-speed water entry of a cylinder using fluid–structure interaction method. *Appl. Ocean Res.* 101, 102285.
- Takami, T., Matsui, S., Oka, M., Iijima, K., 2018. A numerical simulation method for predicting global and local hydroelastic response of a ship based on CFD and FEA coupling. *Mar. Struct.* 59, 368–386.
- Tang, H.Y., Zhang, X.K., Ren, H.L., Yu, P.Y., 2020. Numerical study of trimaran motion and wave load prediction based on time-domain Rankine-Green matching method. *Ocean Eng.* 214, 107605.
- Terziev, M., Tezdogan, T., Inceci k, A., 2020. Application of eddy-viscosity turbulence models to problems in ship hydrodynamics. *Ships Offshore Struct.* 15 (5), 511–534.
- Tezdogan, T., Inceci k, A., Turan, O., 2016. Full-scale unsteady RANS simulations of vertical ship motions in shallow water. *Ocean Eng.* 123, 131–145.
- Wang, X.L., Gu, X.K., Temarel, P., Hu, J.J., 2016a. Investigation of springing in ship structures using experimental methods and 3-D hydroelastic theory. *J. Mar. Sci. Technol.* 21, 271–281.
- Wang, S., Guedes Soares, C., 2013. Slam induced loads on bow-flared sections with various roll angles. *Ocean Eng.* 67, 45–57.
- Wang, S., Guedes Soares, C., 2016a. Experimental and numerical study of the slamming load on the bow of a chemical tanker in irregular waves. *Ocean Eng.* 111, 369–383.
- Wang, S., Guedes Soares, C., 2016b. Stern slamming of a chemical tanker in irregular head waves. *Ocean Eng.* 122, 322–332.
- Wang, S., Guedes Soares, C., 2017. Review of ship slamming loads and responses. *J. Mar. Sci. Appl.* 16 (4), 427–445.
- Wang, S., Karmakar, D., Guedes Soares, C., 2016b. Hydroelastic impact of a horizontal floating plate with forward speed. *J. Fluids Struct.* 60, 97–113.
- Wang, J.H., Wan, D.C., 2020. Application progress of computational fluid dynamic techniques for complex viscous flows in ship and ocean engineering. *J. Mar. Sci. Appl.* 19 (1), 1–16.
- Wang, Y., Wu, W., Guedes Soares, C., 2020. Experimental and numerical study of the hydroelastic response of a River-Sea-Going container ship. *J. Mar. Sci. Eng.* 8 (12), 978.
- Watanabe, I., Keno, M., Sawada, H., 1989. Effects of bow flare shape to the wave loads of a container ship. *J. Soc. Nav. Archit. Japan* 166, 259–266.
- Wu, Y.S., 1984. Hydroelasticity of Floating Bodies (Doctoral Thesis). Brunel University, London, UK.
- Xie, H., Liu, F., Liu, X.Y., Tang, H.Y., 2020. Numerical prediction of asymmetrical ship slamming loads based on a hybrid two-step method. *Ocean Eng.* 208, 107331.
- Zhang, L., Zhang, J.N., Shang, Y.C., 2021. A practical direct URANS CFD approach for the speed loss and propulsion performance evaluation in short-crested irregular head waves. *Ocean Eng.* 219, 108287.
- Zhu, S., Wu, M., Moan, T., 2011. Experimental investigation of hull girder vibrations of a flexible backbone model in bending and torsion. *Appl. Ocean Res.* 33, 252–274.